Ceramics International xxx (xxxx) xxx

Contents lists available at ScienceDirect

Ceramics International

journal homepage: www.elsevier.com/locate/ceramint

One-step electrochemical synthesis of γ-Fe_2O_3@MIL-88a magnetic composite for heterogeneous Fenton-like catalysis

Andrey A. Kuzharov [a], Maksim A. Gritsai [a], Vera V. Butova [a,*], Mikhail A. Soldatov [a], Vladimir A. Polyakov [a], Polina A. Rud [a], Yury V. Rusalev [a], Stanislav P. Kubrin [b], Victor A. Roldugin [a], Alexander L. Trigub [c], Alexander V. Soldatov [a]

[a] The Smart Materials Research Institute, Southern Federal University, Sladkova 178/24, Rostov-on-Don, 344090, Russian Federation
[b] Research Institute of Physics, Southern Federal University, 194, Stachki avenue, Rostov-on-Don, 344090, Russian Federation
[c] National Research Centre "Kurchatov Institute", 1, Akademika Kurchatova sq., Moscow, 123182, Russian Federation

A B S T R A C T

We report a new one-step room-temperature electrochemical synthesis of γ-Fe_2O_3@MIL-88a magnetic composite. Anode from metallic iron was used as Fe-source. We did not use any toxic or hazardous solvents. A careful, comprehensive characterization of the obtained material was applied, including a synchrotron experiment. The γ-Fe_2O_3@MIL-88a composite comprised diamond-like MIL-88a crystals of 100–300 nm covered with γ-Fe_2O_3 nanoparticles. This component provided a magnetic response to the synthesized material. Moreover, γ-Fe_2O_3 nanoparticles boosted semiconductor MOF crystals. As a result, the γ-Fe_2O_3@MIL-88a composite demonstrated superior photocatalytic performance toward methylene blue degradation. MIL-88a crystals acted as photo-Fenton catalysts activating H_2O_2 decomposition with the production of active •OH radicals. Easy magnetic separation and visible-light activated photocatalytic properties make γ-Fe_2O_3@MIL-88a composite a promising system for removing organic dyes from contaminated water according to the photo-Fenton process.

1. Introduction

Metal-organic frameworks are porous materials with great structural diversity [1–3]. They comprise individual metallic centers or clusters of metal ions coordinated with non-metals (oxygen, nitrogen, and so on) [4,5]. These elements are designated as secondary building units. Organic molecules – linkers – bond these elements together and form a crystalline structure. So, crystal structure determines the size and shape of pores, while SBUs and linkers contribute active centers and functional groups for pore surface decoration. Monodisperse tunable pores with various functionalities provide the success of MOFs in such fields as gas sorption and separation [6–10], drug delivery [11–14], water and air purification [15–18], sensing [19,20], electrodes and supercapacitors [21–23], etc.

Among others, catalysis is one of the essential areas of MOF application [24–26]. Highly porous MOFs are widely used as support for catalytic nanoparticles [27–32]. The other option is available catalytic centers which provide catalytic properties to the whole MOF scaffold [17,33]. One of such MOFs is MIL-88a.

MIL-88a is constructed from Fe^{3+} ions and fumaric acid (Fig. 1). The crystal structure of MIL-88a has hexagonal symmetry with a P −62c (190) space group. Linker – fumaric acid – is a non-linear molecule that can rotate around σ-bonds with iron [34–36]. It results in flexibility of the structure. During the activation process or as a result of the solvent exchange, open modification with accessible pores transforms into a closed one. It leads to changes in pore volume and size of apertures in the pores, lattice constants, and XRD patterns [37]. Fe^{3+} ions are octahedrally coordinated with six oxygen atoms. Four of them come from carboxylic groups of linkers, one oxygen is the bridge and common for all tree metallic ions in SBU, and one oxygen belongs to a water molecule. The last one is temporal and can be substituted or removed during post-synthetic sample treatment.

Synthesis of most Fe-based MOFs occurs in toxic solvents. For instance, DMF was used as a solvent for production MIL-53 [38], MIL-88b [39], MIL-125 [40], MIL-101 [41]. On the other hand, MIL-88a can be obtained in a water medium. Available Fe-sites and an energy gap of approximately 2.2 eV make MIL-88a a promising photocatalyst working under visible light irradiation [42]. Moreover, MIL-88a promotes properties of another photocatalysts, such as g-C_3N_4 [42], BiOBr/$SrFe_{12}O_{19}$ [43], MoS_2 [44] etc. Finally, the flexibility of the MIL-88a structure is favorable for mass transfer because it simplifies access to the Fe-sites [45]. Thus, MIL-88a and composites with this MOF were applied as Fenton catalysts for environmental remediation from such pollutants as phenol [46–48], bisphenol A [49,50], tetracycline hydrochloride

* Corresponding author.
E-mail address: vbutova@sfedu.ru (V.V. Butova).

https://doi.org/10.1016/j.ceramint.2022.08.076
Received 25 April 2022; Received in revised form 21 July 2022; Accepted 7 August 2022
Available online 26 August 2022

[51], tris-(2-chloroisopropyl) phosphate [52], salicylic acid [53], and azomethine dyes [50,54–58].

In general, synthesis conditions significantly affect the morphology of MIL-88a particles, which are varied from cubic to rod-like [36,59]. The most common and straightforward method for MIL-88a synthesis is hydrothermal, which results in rod-like crystals [52]. MW-heating and/or organic solvents lead to the formation of diamond or spindle-like nanoparticles [36,47]. The morphology of particles affects the catalytic properties of MIL-88a [47]. The body of MIL-88a crystal comprises (100) edges, which are terminated with (101) ends. The (100) surface possesses a low reaction energy barrier for generating •OH, as confirmed by the DFT method. Rod-like crystals have elongated (100) surfaces, while (101) facets dominate diamond-like particles. The more exposed (100) surface of rod-like MIL-88a enhances H_2O_2 absorption and promotes phenol degradation [47]. Wenxiu Huang et al. applied MIL-88a rod-like particles to phenol degradation [48]. The authors proposed coating MOF with perylene-3,4,9,10-tetracarboxylic diimide to reduce MIL-88a deactivation and increase the stability of the material in an acidic medium. The same group in a recent article reported g-C_3N_4 introduction to MIL-88a via ball milling. The authors claimed that both g-C_3N_4 and MIL-88a absorb photons under visible light. It led to the redistribution of electrons on the valence and conductance bands of composite components. Consequently the efficient separation of the photo-generated electron-hole pairs increased the phenol degradation rate [46]. MIL-88a was also applied for dye degradation [54–58]. Gangli Ren et al. reported ZnO-boosted rod-like MIL-88a crystals for methylene blue decomposition [54]. The membranes with MIL-88a and graphene oxide were proposed for water treatment [55,57,58].

Although the rod-like shape of MIL-88a crystals is considered preferable for Fenton-like catalysis, synthesizing small particles with such a shape is rather challenging. In most cases, the length of rod-like crystals is about a few μm [46,52–54]. However, nanoparticles offer a larger active surface for catalytic transformations. Huifen Fu et al. proposed room temperature synthesis of MIL-88a in the water-ethanol mixture to obtain spindle-like particles [50]. The authors compared MIL-88a with the particle size of 500 and 1000 nm. They claimed that smaller crystals exhibited better photo-Fenton catalytic performance toward rhodamine B and bisphenol A removal under visible light irradiation.

Magnetic properties give an excellent advantage to the heterogeneous catalytic process. Many researchers used MIL-88a as a precursor for the production of magnetic nanoparticles in carbon support [60–64]. However, pyrolysis destroys the MIL-88a structure. An alternative way is a multistep synthesis of composites comprising magnetic nanoparticles and MIL-88a. Yi Liu et al. reported the synthesis of Fe_3O_4@-MIL-88a composite [65]. First, they obtained rod-like MIL-88a particles via hydrothermal synthesis. Then they added them to the reaction mixture for Fe_3O_4 synthesis by coprecipitation technique. Fe_3O_4@-MIL-88a composites were applied for Bromophenol Blue degradation. The simple magnetic separation allowed multiple recycling of the synthesized catalyst.

Additionally, to magnetic separation options, iron oxides can alternate the photocatalytic properties of the composite material. Such iron oxides as hematite, maghemite, and magnetite demonstrate semiconductor photocatalytic performance as Fenton-catalysts [66]. γ-Fe_2O_3 is an n-type semiconductor. Its bandgap of 2.2 eV allowed absorbing light with wavelengths up to 560 nm [67]. In addition, due to the narrow bandgap of Fe_2O_3, it can be utilized as a sensitizer of such photocatalysts as TiO_2 [68], graphene oxide [69], biochar [70], SiO_2 [71].

In this way, one-pot synthesis of magnetic composite with MIL-88a nanoparticles is an urgent task. Such composite is a promising heterogeneous catalyst, which could be magnetically separated for recycling. It was reported that nucleation rate dramatically affects the size and morphology of MIL-88a crystals [36,59]. Electrosynthesis provides some advantages over traditional solvothermal methods. For instance, MOFs are produced electrochemically in mild conditions and in short synthesis times. Additionally, the electrochemical process offers precise control of synthetic conditions, including the rate of Fe-ions supply [72]. Using metallic electrodes as a source of metallic ions instead of their salts is more environmentally friendly. Moreover, it allows direct deposition of MOFs on substrates with real-time control of the structure and thickness of the layer [73]. Several MOFs were successfully obtained via the electrochemical procedure (Table S1 in SI) [74]. Nicolo Campagnol et al. reported the electrochemical deposition of the Fe-MIL-100 thin layer for the first time in 2013 [75]. This MOF is constructed from Fe^{3+} ions and 1,3,5-benzene tricarboxylic linkers (BTC). The authors used an iron plate as an anode and an iron substrate as a cathode in a high-pressure,

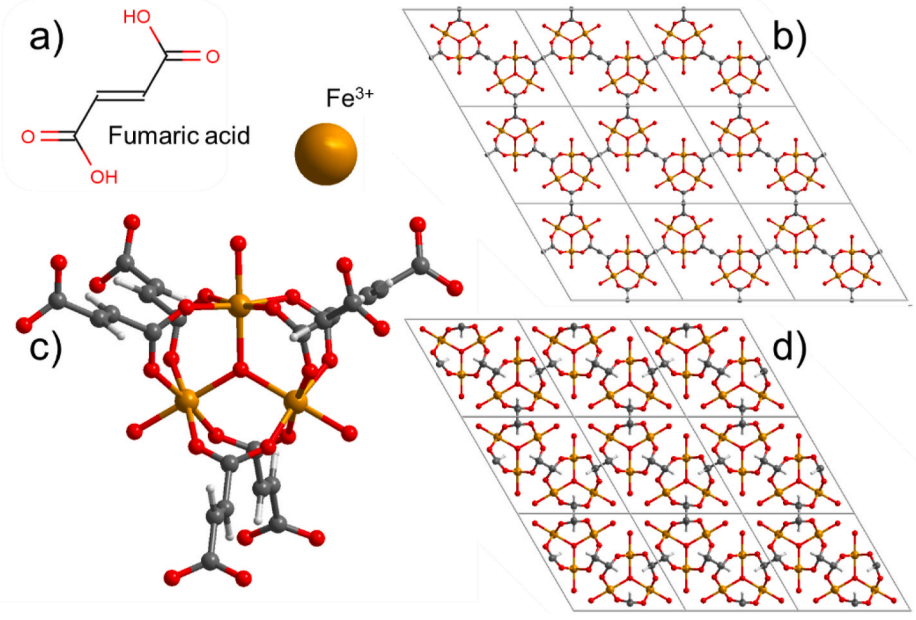

Fig. 1. (a) Structural formula of MIL-88a linker – fumaric acid and representation of Fe^{3+} ions for other parts. Model of the structure of MIL-88a in open (b) and closed (d) modifications. (c) SBU of MIL-88a. Orange spheres represent Fe^{3+} ions, gray ones stand for carbon, red ones show oxygen, and light-gray ones designate hydrogen.

high-temperature electrochemical cell. The mixture of water and ethanol was applied as a solvent for the BTC linker without additives such as mineral acids or ionic liquids. Temperature and current density were optimized to obtain a fine layer of MIL-100 on Fe-substrate. The material was tested for methanol storage and separation. In the recent article, electrochemical synthesis of Fe-MIL-100 was proposed in mild conditions [76]. The authors used the ionic liquid additive (1-Dodecyl, 3-Methyl Imidazolium Chloride) and two iron electrodes. After 90 min of electrosynthesis at 40 °C, voltage 30 V (current 0.9 A) MIL-100 brown precipitate was obtained. The synthesized material was applied for pH-responsive drug delivery. A combination of Fe^{3+} ions and terephthalic acid (BDC) has been shown to generate at least three MOFs: MIL-53, MIL-88b, and MIL-101. It was reported that controlled electrochemical oxidation of Fe^{2+} to Fe^{3+} in the presence of BDC induced MOF formation with the control of the phase and quality of the material [77]. The authors utilized a one-compartment cell for controlled oxidation of Fe^{2+} ions from $FeCl_2$ in DMF. The additive of 2,6-Lutidine was used as a proton scavenger. In this study, the authors obtained Fe-MIL-101 and Fe-MIL-101-NH_2 both in powder and as a layer on a carboxy-functionalized indium tin oxide substrate. However, there are no reports of electrochemical synthesis of MIL-88a and magnetic composites with it to the best of our knowledge.

We report here a new strategy for one-pot electrochemical production of magnetic composite γ-Fe_2O_3@MIL-88a. The obtained material was comprehensively characterized and applied for dye degradation via the photo-Fenton process.

2. Experimental section

Fumaric acid ($H_4C_4O_4$), potassium chloride (KCl), sodium chloride (NaCl), and ethanol (C_2H_5OH) were purchased from commercial suppliers and used without further purification. Deionized (DI) water (18 MΩ cm) was obtained from the Simplicity UV water purification system.

2.1. Electrochemical synthesis of γ-Fe_2O_3@MIL-88a

The electrochemical cell for obtaining γ-Fe_2O_3@MIL-88a consisted of two iron electrodes (Alfa Aesar) with 99.995% pure metal. 2.5 × 2.5 cm Fe-plates were immersed in the electrolyte for 2 cm. So 0.5 cm of electrodes were dry and used for connection to galvanostat.

The volume of the electrolyte was 150 ml. The volume ratio of electrolyte components was 50% H_2O and 50% ethanol. The concentration of the linker (fumaric acid) was 0.02 M. Potassium chloride (0.559 g) was added to the electrolyte solution to increase the conductivity. Electrolysis was carried out using a P-20x galvanostat (Electrochemical Instruments). The synthesis optimization was carried out by varying the current strength and the electrolysis time (Table S2, Fig. S1, Fig. S2 in SI). Based on XRD, FTIR, and TEM studies, the optimal synthesis parameters were determined for obtaining nano-sized crystals with diamond-like morphology. They are the following: voltage: V = 15 V, the current density I = 12 mA cm^{-2}, and the electrolysis time of 30 min with stirring. After the end of the synthesis, the obtaining dispersions were centrifuged, washed with water, centrifuged again, and dried for 18 h.

2.2. Electrochemical synthesis of γ-Fe_2O_3

Magnetic γ-Fe_2O_3 nanoparticles were obtained by a method similar to the electrochemical synthesis of the γ-Fe_2O_3@MIL-88a composite. The only difference was that the linker (fumaric acid) was not added to the reaction mixture. And sodium chloride (0.877 g) was added to the electrolyte solution to increase the conductivity instead of potassium chloride.

2.3. Synthesis of microcrystalline MIL-88a

Microcrystalline MIL-88a (μMIL-88a) was obtained by the following method [64]. 0.6964 g of fumaric acid was dissolved in 150 ml of water. 1.6218 g of $FeCl_3{\cdot}6H_2O$ was dissolved in 10 ml of water and was added to the fumaric acid solution. The residuals of $FeCl_3{\cdot}6H_2O$ were mixed with an additional 10 ml H_2O and transferred to the reaction mixture. The total volume of the solution was 170 ml. It was placed in an oven for 19 h at a temperature of 70 °C. Orange precipitate was washed one time with water, one time with ethanol, and dried.

2.4. Photocatalytic studies

Photocatalytic studies were carried out in transmission geometry on a double-beam UV2600 spectrometer (Shimadzu, Kyoto, Japan) equipped with 10 mm quartz cells.

596 μl of a 30% hydrogen peroxide solution was added to 100 ml of 1 mg/ml methylene blue solution. After that, 20 mg of the respective catalyst was added to the mixture (see Table 2). The catalytic process was performed with vigorous stirring under white light irradiation (Table 2, conditions (1), (@-2), (@-4), (μ-2), (μ-4), (γ-2)) or in darkness (Table 2, conditions (@-1), (@-3), (μ-1), (μ-3), (γ-1)). Every 10 min, an 2 ml aliquot was taken from the solution, and its absorbance spectrum was measured. The reference experiment was carried out in the same conditions under white light irradiation without a catalyst (see Table 2, conditions (1)).

2.5. Characterization

Fourier Transform Infrared (FTIR) spectra were obtained on a Vertex 70 spectrometer (Bruker, Germany) in ATR (Attenuated total reflectance) geometry using an MCT detector and a Bruker Platinum ATR accessory. The spectra were measured from 5000 to 500 cm^{-1} with a resolution of 1 cm^{-1} and 64 scans. The reference spectrum was collected in air.

X-ray powder diffraction (XRPD) patterns were recorded on a D2 Phaser diffractometer (Bruker AXS, Germany) operating at an acceleration voltage of 30 kV and a tube current of 10 mA generating Cu K_α radiation (λ_1 = 1,54056 Å, λ_2 = 1.544390 Å). The data were collected with a step size of 0.01° and a counting time of 2 s per point from 5° to 70° (2θ). Rietveld refinement was performed using FullProf software [78].

Thermogravimetric analysis (TGA) and differential scanning calorimetry (DSC) was measured using an STA 449 F5 Jupiter instrument (Netzsch, Germany) by heating the sample to 800 °C at a rate of 5 °C per minute. The measurements were carried out in a corundum crucible in the airflow.

To determine the shape and size of the synthesized crystallites, images were collected using a Tecnai G2 transmission electron microscope (FEI, Netherlands).

Specific surface areas were calculated using the Brunauer - Emmett - Teller (BET) model from nitrogen adsorption isotherms measured on a Micromeritics ASAP (Accelerated Surface Area and Porosimetry) ASAP 2020 (Micromeritics). The hydrogen capacity was calculated from the hydrogen adsorption thermals measured at 77 K. Samples were activated at 150 °C for 10 h under a dynamic vacuum before measurements.

The spectra of γ-Fe_2O_3@MIL-88a were recorded using the equipment of the Kurchatov Synchrotron Radiation Source (National Research Center Kurchatov Institute, Moscow, Russia). The synchrotron radiation source was a storage ring with an electron beam energy of 2.5 GeV and a current in the range of 50–120 mA. The experiments were performed at the "Material structure" beamline [79]. Channel-cut Si(111) single crystal monochromator was used for monochromatization of the X-ray beam with an energy resolution $\Delta E/E = 2 \times 10^{-4}$. All the samples were ground finely, mixed with cellulose, and pressed into pallets. The XAS spectra at Fe K-edge were registered in transmission mode. The X-ray

intensity was measured using three tandem ionization chambers filled with N_2. The studied sample was placed between the 1st and 2nd chambers and the reference between the 2nd and 3rd chambers. The integration time in every energy point was set to 1 s. In each case, up to three spectra were collected for their further averaging. Background subtraction and spectra normalization was carried out using the Athena program of the IFEFFIT software package [80]. A pre-edge background was subtracted from the entire spectrum. The obtained spectra were normalized using fitted EXAFS data beyond the near-edge structure.

Magnetic measurements were carried out on a Lakeshore VSM 7404 magnetometer. Magnetization curves were measured at room temperature in the field range from −19 kOe to 19 kOe. There are at least 160 points for each measurement with a shutter speed of 10 s per point.

Mössbauer spectra were measured using an MS1104Em spectrometer equipped with the CCS-850 helium refrigerated cryostat chamber (Janis Inc.). ^{57}Co in the Rh matrix was used as a source of gamma quanta. Model decoding of the spectra was carried out using the SpectrRelax software [81]. Isomer shifts were calculated relative to metallic α-Fe.

3. Results and discussion

3.1. Electrochemical synthesis

In this work, the electrochemical method was used for the first time for the one-step preparation of γ-Fe_2O_3@MIL-88a composite. During electrochemical oxidation, the iron anode was dissolved to provide iron ions. The electrodes were placed in a solution of fumaric acid, which interacted with the iron ions to form γ-Fe_2O_3@MIL-88a precipitate. The electrochemical cell and the formation mechanism of γ-Fe_2O_3@MIL-88a are shown in Fig. 2 (a photo of the electrochemical cell is provided in SI Fig. S3a).

The crystal lattice of MIL-88a contains Fe^{3+} ions. However, anode dissolution provided both Fe^{3+} and Fe^{2+} ions. We collected and studied supernatant to prove this statement. The solution of $K_3[Fe(CN)_6]$ was added to one part of the liquid. It turned the color to the dark blue indicating presence of Fe^{2+} ions. The other part was tested with $K_4[Fe(CN)_6]$ solution. Its additive resulted in the formation of dark blue $KFe[Fe(CN)_6]$ precipitate, which implied Fe^{3+} ion presence in the supernatant (see Fig. S3b in SI). Thus, metallic iron was first oxidized to ferrous ions, and then Fe^{2+} ions were oxidized to ferric ions:

$$A: Fe^0 - 2\,\bar{e} = Fe^{2+}$$

$$Fe^{2+} - \bar{e} = Fe^{3+}.$$

In this case, the release of gaseous hydrogen and partial reduction of iron ions occurred simultaneously at the cathode:

$$C: 2H^+ + 2\,\bar{e} = H_2\uparrow \quad xFe^{2+} + yFe^{3+} + (2x+3y)\bar{e} = (x+y)Fe^0.$$

The iron ions moved from the anode to the cathode region. Part of them participated in forming γ-Fe_2O_3 oxide. The other part of Fe^{3+} ions interacted with fumaric acid in the solution (Fig. 2c):

$$3Fe^{3+} + 3H_4C_4O_4 = Fe_3O(C_4H_2O_4)_3(OH) + 9H^+.$$

Both competitive processes - the formation of γ-Fe_2O_3 and MIL-88a – run parallel. As a result, the surface of diamond-like MIL-88a crystals was decorated with γ-Fe_2O_3 nanoparticles forming γ-Fe_2O_3@MIL-88a composite. The obtained material was collected using a permanent magnet (Fig. 2d and e).

3.2. Characterization

TEM images were collected to determine the shape and size of the synthesized particles. The μMIL-88a sample comprised rod-like crystals with an average width of 400 nm and length of 1–4 μm (Fig. S4 in SI). The γ-Fe_2O_3@MIL-88a sample contained 100–350 nm in length and 100–200 nm in width (Fig. 3). The diamond-like crystals were covered by small dense nanoparticles.

We propose that the initial step of electrochemical synthesis was the formation of iron oxide nuclei. An energy barrier exists for nucleation, and thus a supersaturation of the solution is required to initiate the crystallization [21]. Therefore, a certain time was needed to accumulate nuclei of Fe_xO_y species. According to high-resolution TEM images, control electrochemical synthesis without fumaric acid resulted in magnetic 8–9 nm nanoparticles of the γ-Fe_2O_3 sample (Fig. S5 in SI). It allowed us to conclude that these magnetic nanoparticles on the surface of MIL-88a crystals are γ-Fe_2O_3 (Fig. 3 d,f). They have a size distribution of 3–10 nm.

The second stage is crystal growth. The rate of this process is not equal for different crystallographic planes. As a result, the square crystals grow to form diamond-like ones. Further expansion of particles results in a rod-like shape. It is typical for MIL-88a, synthesized in a water medium [52]. We observed such morphology for the μMIL-88a sample (Fig. S4 in SI). Although water-based synthesis is preferred, obtaining MIL-88a diamond-like nanoparticles has only been possible using toxic solvents such as DMF [36,59]. To the best of our knowledge, the proposed synthesis is the first technique that allowed the formation of diamond-like γ-Fe_2O_3@MIL-88a composite nanoparticles in a non-toxic water-based medium.

The crystallinity and phase composition of μMIL-88a, γ-Fe_2O_3@MIL-

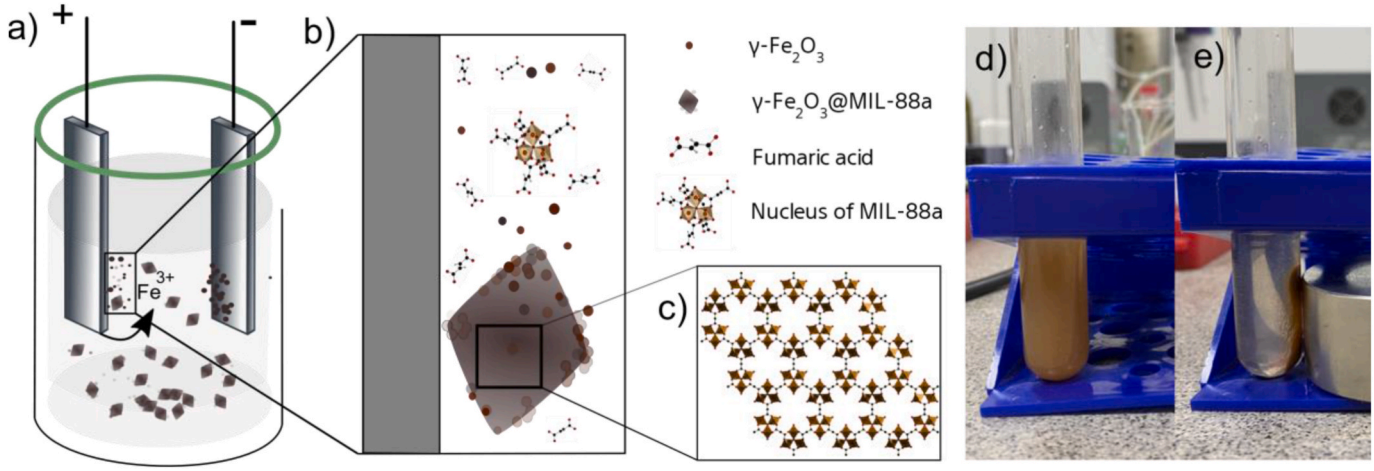

Fig. 2. (a) An electrochemical cell and (b) the formation mechanism of γ-Fe_2O_3@MIL-88a: iron ions link with molecules of fumaric acid to form the nuclei of MIL-88a crystals, from which γ-Fe_2O_3@MIL-88a structure is formed (c). (d) The reaction mixture after synthesis, (e) the reaction mixture by exposure to a magnetic field.

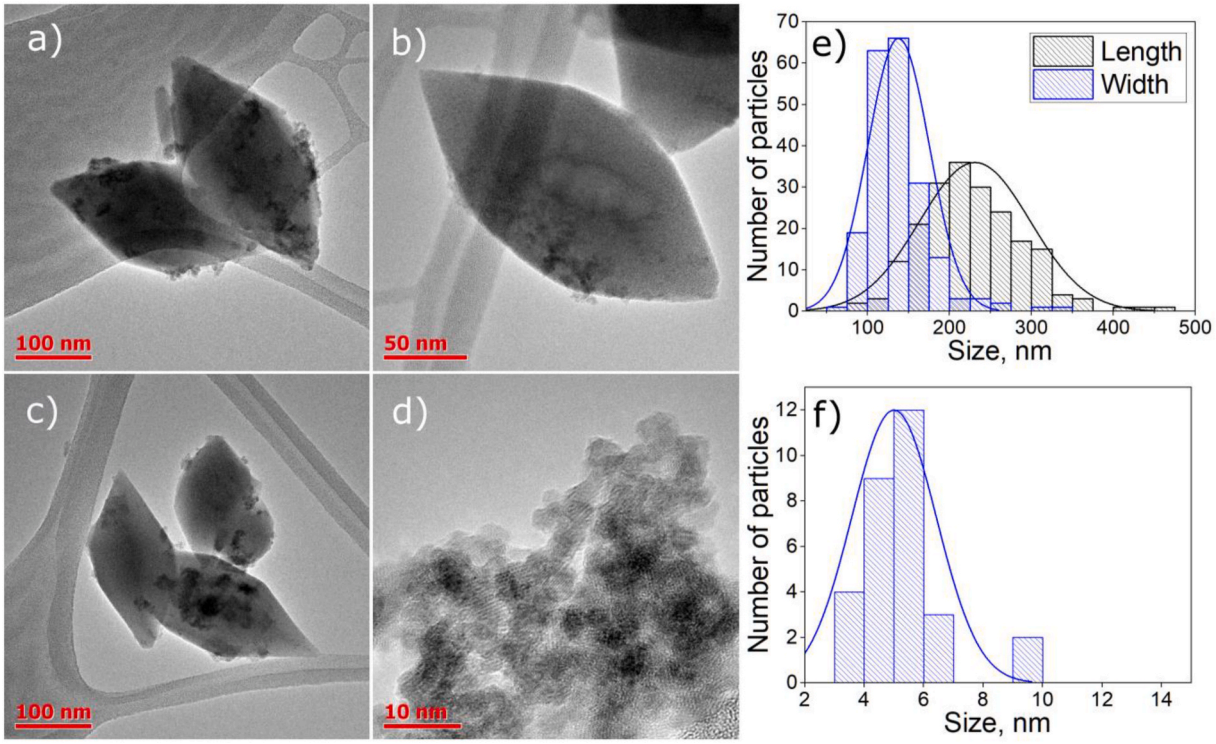

Fig. 3. TEM images (a–c) of γ-Fe_2O_3@MIL-88a composite, (d) γ-Fe_2O_3 nanoparticles on the surface of MIL-88a crystals, and size distribution (e) of MIL-88a and (f) γ-Fe_2O_3 nanoparticles.

88a and γ-Fe_2O_3 were determined by X-ray diffraction. The corresponding results are shown in Fig. 4. XRD pattern of γ-Fe_2O_3 revealed a standard set of well-defined peaks at 30.2°, 35.6° and 43.3°, corresponding to the (220), (311), and (400) reflections of the maghemite structure, respectively (COD #9006316). Rietveld refinement was carried out to investigate structural features further. The lattice parameter of iron oxide was 8.36 Å, and the average crystallite size was about 8 nm. Moreover, some additional peaks were detected at 31.8° and 45.6° (Fig. S6 in SI). They were assigned to a sodium chloride phase (COD #2311042). Such impurity came from a NaCl added to the solution for better conductivity [50].

The diffractogram of μMIL-88a matched with the previously reported MIL-88a diffraction patterns, showing the well-known group of peaks at 9.0°, 10.8°, and 11.9°, corresponding to the reflections with indices (100), (101), and (002), respectively [34,37,60,82]. The ratio of the intensities of Bragg reflections (100) and (101) indicated the rod-like morphology of particles in agreement with TEM data and reported results [47,60,83]. According to the Rietveld structural analysis, the lattice parameters of μMIL-88a were estimated as a = b = 11.35 Å and c = 14.88 Å. It corresponds to the result of the thermo-diffraction analysis for the as-synthesized structure provided by Mellot-Draznieks et al. [37]. It is well known that MIL-88a has a very flexible swelling structure [34,84], and its pores can be either open or closed. Such behavior is accompanied by a variety of lattice parameters over an extensive range, which leads to the change in the reciprocal position of the reflections. The more comprehensive investigation of the other visible peaks, especially ones with low intensity, is complicated, and unwanted misconceptions can be made. For example, the analysis of a group of reflections at 20–25° (2θ) failed because the separation of MIL-88a contribution and possible phases of iron oxides can not be held clearly (Fig. S7 in SI).

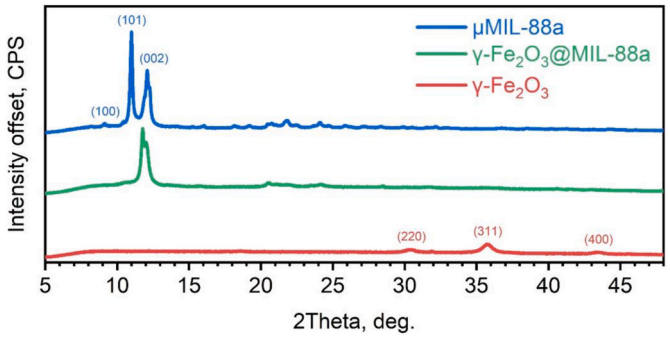

Fig. 4. XRD patterns of μMIL-88a, γ-Fe_2O_3@MIL-88a, and γ-Fe_2O_3. The patterns were shifted along the y-axis for better representation.

Comparison of the diffraction pattern of γ-Fe_2O_3@MIL-88a composite with those of pristine μMIL-88a and γ-Fe_2O_3 led us to the following results. The composite material showed lower crystallinity than pristine μMIL-88a because most of the peaks corresponding to the MOF structure were weaker. Moreover, the (100) reflection of MIL-88a was not detected further, and the most intense (101) peak turned into a very weak additional feature at the tail of the (002) peak. Thus the relative intensity of (100) and (101) reflections remained the same, indicating a diamond morphology of the MOF. Interestingly, the (002) reflection remained very similar in shape but shifted for about 0.1° towards a lower scattering angle. It may be assumed that all these changes were caused by the partly amorphized structure resulting from the contribution of magnetic iron oxide nanoparticles [85]. On the other hand, γ-Fe_2O_3 particles were pretty small, and TEM images implied their low contribution to the composite material. For this reason, direct visual observation of the iron oxide phase in γ-Fe_2O_3@MIL-88a composite by XRD was hampered, and only a weak trace of the (311) reflection was detected at about 35.9° (Fig. S8 in SI). According to the Rietveld refinement, the lattice parameters of the γ-Fe_2O_3@MIL-88a composite were estimated as a = b = 11.81 Å and c = 15.0 Å. Similar to the case of pristine γ-Fe_2O_3, additional peaks were observed at 28.5° and 40.6°, which correspond to the KCl impurity phase.

Fig. 5 shows FTIR spectra for γ-Fe_2O_3 nanoparticles, γ-Fe_2O_3@MIL-

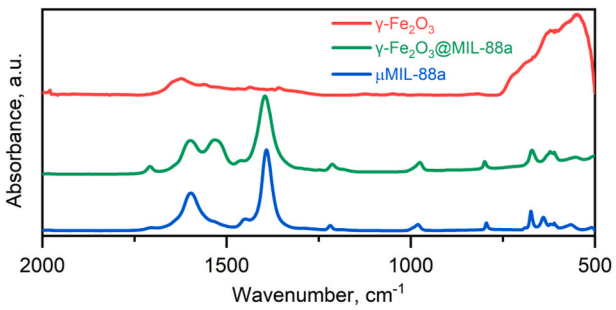

Fig. 5. FTIR spectra for γ-Fe_2O_3 nanoparticles (red), γ-Fe_2O_3@MIL-88a composite (green), and μMIL-88a (blue).

88a composite, and μMIL-88a. Two pronounced and twin peaks in spectra of γ-Fe_2O_3 nanoparticles at 549 cm^{-1} and 621 cm^{-1}, of γ-Fe_2O_3@MIL-88a at 551 cm^{-1} and 611 cm^{-1}, and of μMIL-88a at 566 cm^{-1} and 641 cm^{-1} were assigned to the iron-oxygen bond (Fe–O) [86]. The composite had a more pronounced and intense double peak, which indicated a higher concentration of iron in the composite than in μMIL-88a. The peaks detected at 671 cm^{-1} and 673 cm^{-1} for γ-Fe_2O_3@MIL-88a and μMIL-88a, respectively, corresponded to the carboxylate group (COO^-) ligands [87,88]. Distinct peaks at 800 cm^{-1} and 796 cm^{-1} were assigned to the bending vibration C–H [89,90]. The peaks at 975 cm^{-1}, 982 cm^{-1} and 1213 cm^{-1}, 1218 cm^{-1} were explained by the stretching vibration C–C and C=C, respectively [91, 92]. The characteristic asymmetric and symmetrical stretching frequency C=O at 1601 cm^{-1}, 1598 cm^{-1} and 1395 cm^{-1}, 1392 cm^{-1}, respectively, correlated with the coordinated carboxylate in fumaric acid [56]. This data confirmed the presence of iron and organic ligands, which fully corresponded to the chemical composition of MIL-88a. The γ-Fe_2O_3@MIL-88a composite was synthesized in an aqueous solution. Thus, a broad peak in the region between 3200 and 3400 cm^{-1} was due to adsorbed water. The presence of water adsorbed by γ-Fe_2O_3@-MIL-88a composite was confirmed using thermogravimetric analysis.

The TGA and DSC curves are shown in Fig. 6. The first stage of weight loss was observed in the temperature range of 25–150 °C. It corresponded to the release of water from the MIL-88a pores. The second weight loss was associated with an exothermic process of the framework collapse. Positive peaks were observed in the DSC curves of both samples in the temperature range of 200–500 °C. The step in the TGA curve and the peak in the DSC curve of μMIL-88a at 250–450 °C corresponded to

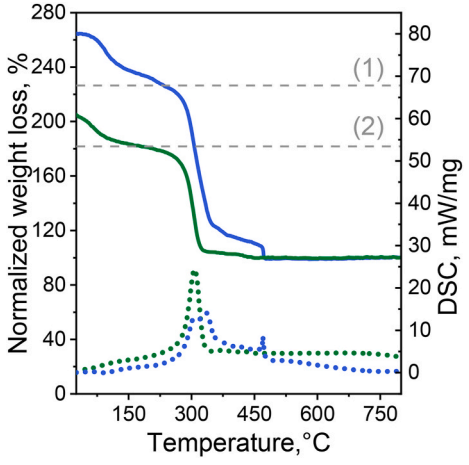

Fig. 6. TGA (solid lines) and DSC (dotted lines) curves for γ-Fe_2O_3@MIL-88a composite (green lines) and μMIL-88a (blue lines). Dashed gray lines represent the calculated position of the plateau according to the formula unit $Fe_3O(H_2C_4O_4)_3OH$ (1) and $Fe_3O(H_2C_4O_4)_3OH{\bullet}0.8Fe_2O_3$ (2). TGA curves were normalized.

the formation of iron oxide with carbon shell as solid residual. Further heating led to the formation of pure iron oxide, while the carbon shell interacted with oxygen, producing carbon dioxide. The same non-smooth curves were recorded for the γ-Fe_2O_3@MIL-88a sample. However, the effect was less pronounced. We suppose that it is attributed to less MIL-88a in the composite. Moreover, we expect that nanoparticles of MOF in the γ-Fe_2O_3@MIL-88a sample interacted with oxygen faster due to the larger active surface.

The thermal decomposition of MIL-88a in the airflow corresponds to the following process:

$$2\ Fe_3O(H_2C_4O_4)_3OH + 18\ O_2 = 3\ Fe_2O_3 + 24\ CO_2 + 7H_2O.$$

Theoretical weight loss for MIL-88a is 55.9% according to the formula unit $Fe_3O(H_2C_4O_4)_3OH$. Experimental weight loss for μMIL-88a was very close to this value. Contrary, the γ-Fe_2O_3@MIL-88a sample exhibited a lower weight loss of 45% due to the presence of γ-Fe_2O_3 nanoparticles in the composition. In this case, iron oxide nanoparticles did not produce any gaseous products while heating in the air. Therefore, γ-Fe_2O_3 nanoparticles in composite led to a more significant weight of solid residual after decomposition. According to experimental weight losses and formula unit of MIL-88a fixed as $Fe_3O(H_2C_4O_4)_3OH$, we proposed the following compositions for synthesized samples: μMIL-88a – $Fe_3O(H_2C_4O_4)_3OH{\cdot}5H_2O$, γ-$Fe_2O_3$@MIL-88a – $Fe_3O(H_2C_4O_4)_3OH{\cdot}0.8Fe_2O_3{\cdot}4H_2O$.

The specific surface areas of the γ-Fe_2O_3@MIL-88a composite and μMIL-88a, according to the BET model, were estimated as 128.5 m^2g^{-1} and 143.9 m^2g^{-1}, respectively (Fig. 7a). Both values are lower than theoretically predicted. According to reported data, the MIL-88a possesses a flexible framework [34,37]. Solvent exchange or evacuation affects the stabilization of open/closed modifications. We suppose that degas pretreatment stabilized the closed-form of MIL-88a, resulting in low BET surface areas. The same was observed previously [47,93,94]. In the IUPAC definition, the shape of μMIL-88a isotherm was assigned to type I. It is typical for microporous materials. On the other hand, the γ-Fe_2O_3@MIL-88a composite demonstrated the isotherm of type II. This shape is specific for non-porous or macroporous systems. We attributed this feature to the contribution of Fe_2O_3 nanoparticles. The pronounced hysteresis loop of the γ-Fe_2O_3@MIL-88a sample was attributed to the capillary condensation of nitrogen in meso-cavities. Its shape corresponded to type H3 in IUPAC notification, typical for plate-like pores. We attributed such cavities to adsorption into spaces between the particles in agglomerates.

We measured hydrogen sorption isotherm for both samples and observed the opposite trend (Fig. 7b). The μMIL-88a sample adsorbed 0.63 wt % of hydrogen at 790 mmHg. The γ-Fe_2O_3@MIL-88a composite exhibited an H_2 capacity of 0.17 wt % at the same pressure. Both N_2 and H_2 physisorption isotherms were measured at 77 K. It is a boiling temperature for nitrogen. Thus, it can be physisorbed onto the solid surface by capillary condensation in the mesopores and a micropore volume filling mechanism. However, hydrogen possesses a critical temperature of 33 K. Thus, at 77 K, its physisorption refers to the monolayer coverage

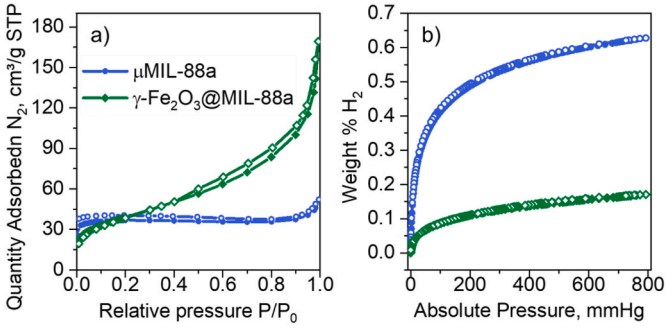

Fig. 7. Nitrogen (a) and hydrogen (b) adsorption-desorption isotherms.

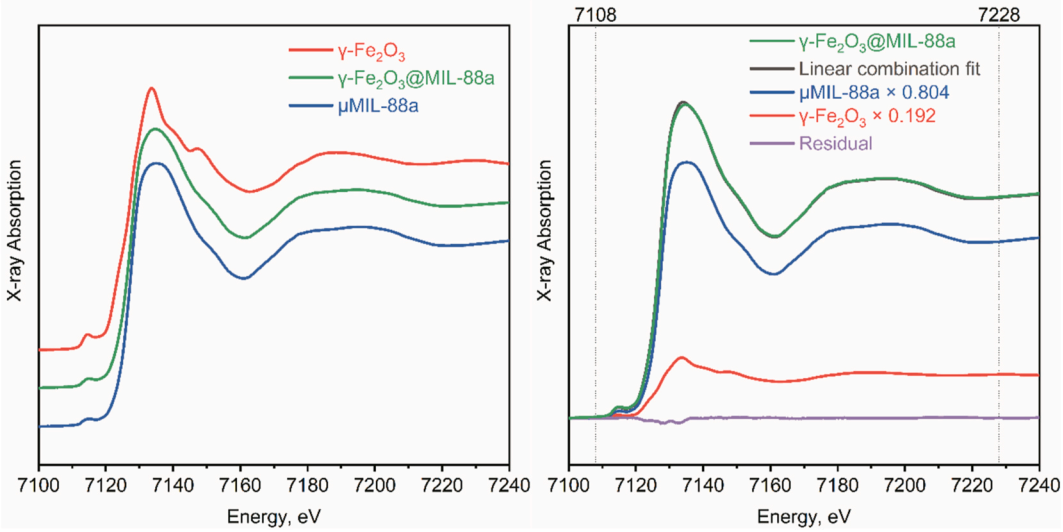

Fig. 8. Left: XANES spectra measured for γ-Fe_2O_3 nanoparticles (red), γ-Fe_2O_3@MIL-88a composite (green), and μMIL-88a (blue). Right: The results of linear combination fit (grey) of γ-Fe_2O_3@MIL-88a composite XANES spectra (green) using two components: γ-Fe_2O_3 nanoparticles (red) and μMIL-88a (blue). The residual is shown in purple. The range of the fit is marked with dash lines at 7108 eV and 7228 eV.

over the solid surfaces without capillary condensation. It explains why the microporous μMIL-88a sample exhibited a higher H_2 capacity than γ-Fe_2O_3@MIL-88a composite with non-porous Fe_2O_3 component and mesopores in agglomerates.

3.3. Magnetic properties

The results of magnetic hysteresis loops measurements for γ-Fe_2O_3 nanoparticles (Fig. S9 in SI), μMIL-88a (Fig. S10 in SI), γ-Fe_2O_3@MIL-88a composite (Fig. S11 in SI) are summarized Table 1.

The μMIL-88a was paramagnetic and did not reach saturation at the maximum field. The paramagnetism of this sample is explained by the fact that iron atoms in the sample do not form particles with a domain structure and are located only at the MOF sites.

The γ-Fe_2O_3 sample comprised magnetic nanoparticles. This sample tended to saturation at the maximum field value. Its magnetization at 19 kOe was estimated at 39.872 emu·g^{-1}. The coercive force of this sample was ~21 Oe, which corresponded to the Fe_2O_3 γ-phase with an average size of less than 9 nm [95,96].

The γ-Fe_2O_3@MIL-88a sample did not reach saturation at the maximum field. It is associated with the composition of the material. It contains mixture of magnetic nanoparticles and paramagnetic crystalline MIL-88a. The magnetization of this sample at 19 kOe was 2.8593. This sample had practically no residual magnetization and an order of magnitude lower coercive force.

3.4. XANES

The Fe K-edge XANES spectra for γ-Fe_2O_3 nanoparticles, γ-Fe_2O_3@-MIL-88a composite, and μMIL-88a are presented in Fig. 8 (left). The rising edge position of the spectra corresponds to the oxidation state of Fe^{3+}. On the one hand, the latter is in agreement with previous MIL-88a XANES studies [97]. On the other hand, it could be an additional argument in favor of the γ-Fe_2O_3 phase for iron oxide nanoparticles which are often confused with another spinel magnetic phase of iron oxide Fe_3O_4 that contains mixed-valence Fe atoms [98]. Although it could be clearly seen that the spectra of γ-Fe_2O_3@MIL-88a composite are quite similar to those of μMIL-88a, the magnetic measurements imply the presence of a magnetic phase in the composite sample. Based on this, it is possible to assume that the γ-Fe_2O_3@MIL-88a composite is formed from the mixture of magnetic γ-Fe_2O_3 nanoparticles phase and μMIL-88a. And thus, the spectra of γ-Fe_2O_3 nanoparticles and μMIL-88a reproduce the pure components that could reproduce the spectrum of composite materials. To check this hypothesis a linear combination fit (LCF) was performed for spectral interpretation.

The quantitative estimation of the atomic percent of Fe atoms that correspond to γ-Fe2O3 nanoparticles and μMIL-88a phases in γ-Fe_2O_3@MIL-88a composite material was performed by linear combination fit XANES spectra (Fig. 8 right). The spectra of γ-Fe_2O_3 nanoparticles and μMIL-88a were used as reference components. The fitting procedure performed in different energy ranges gives similar results. Based on the LCF analysis, it was estimated that more than 80 at% of Fe atoms in γ-Fe_2O_3@MIL-88a composite material correspond to the μMIL-88a phase, and less than 19 at% of Fe atoms correspond to the γ-Fe_2O_3 phase. A rough estimation of wt% for γ-Fe_2O_3 and MIL-88a phases based on LCF results suggests ~10 wt% of γ-Fe_2O_3 phase in a composite material. This estimation shows relevant agreement with magnetization measurements and TGA data discussed above.

Table 1
Magnetic properties of γ-Fe_2O_3 and γ- Fe_2O_3@MIL-88a composite.

Sample	Coercive force Oe	Remanence emu·g^{-1}	Magnetization emu·g^{-1}
γ-Fe_2O_3	20.999	1.7991	39.872
γ-Fe_2O_3@MIL-88a	3.6037	$4.2860 \cdot 10^{-3}$	2.8593

Table 2
Experiments of MB degradation. The k stands for rate constant according to pseudo-first-order (see details in SI Fig. S14b).

Catalyst	MB	H_2O_2	light	k, min^{-1}	
no	+	+	+	no	(1)
γ-Fe_2O_3@MIL-88a	+	–	–	no	(@-1)
	+	–	+	no	(@-2)
	+	+	–	0.0103	(@-3)
	+	+	+	0.0408	(@-4)
μMIL-88a	+	–	–	no	(μ-1)
	+	–	+	no	(μ-2)
	+	+	–	no	(μ-3)
	+	+	+	0.0930	(μ-4)
γ-Fe_2O_3	+	+	–	no	(γ-1)
	+	+	+	no	(γ-2)

3.5. Mössbaer

The Mössbaer spectra of a μMIL-88a sample measured at 300K and 15K are shown in Fig. 9. The spectra are a superposition of two doublets at both temperatures with different quadrupole splitting Δ parameters (Table 2). In the μMIL88a sample, iron ions occupy two non-equivalent crystal positions. The isomer shift values correspond to Fe^{3+} ions in the high-spin state and octahedral environment [99]. The electric field gradient determines quadrupole splitting. In the case of Fe^{3+} ions, the electric field gradient is created by molecular orbital and lattice contributions [100]. Since both positions are in the composition of the same crystal structure, the lattice contribution to the value of Δ will be the same. Thus, the difference in the Δ values of the D1 and D2 doublets is determined by the molecular orbital contribution, which is nonzero in the case of the presence of different ligands in the nearest environment of the Fe^{3+} ions. Probably, the doublet D1 with a smaller value of Δ corresponds to Fe^{3+} ions surrounded by O^{2-} ions. Doublet D2 with a large value of Δ arises from Fe^{3+} ions surrounded by O^{2-} and Cl^{-} ions. The values of the areas of doublets are approximately proportional to the concentration of Fe^{3+} ions in the corresponding states. Since there are two types of the local environment of Fe^{3+} ions, their *f*-factors can differ. Therefore, to estimate the concentrations of Fe^{3+} ions in these states, the values of the areas of doublets at low temperatures should be used. At 15 K, the areas of doublets D1 and D2 approximately coincide.

The Mössbauer spectrum of the γ- Fe_2O_3@MIL-88a sample at room temperature (Fig. 10) also consists of two doublets: D and DS (Table 2). However, at temperatures below 70 K, Zeeman splitting lines appear in the spectra, and the doublet area DS decreases. At temperatures below 55 K, the DS doublet disappears, and the area of the components corresponding to the Zeeman splitting increases. Probably, the DS doublet corresponds to nanoparticles of iron oxide or hydroxide, which exhibit superparamagnetic properties [101]. Suppose the frequency of superparamagnetic relaxation is greater than the frequency of the Larmor precession. In that case, the Zeeman structure of the Mössbauer spectrum of particles collapses into a doublet or singlet at temperatures below the Curie/Néel temperature. A decrease in temperature leads to a decrease in the frequency of superparamagnetic relaxation and a resolution of the Zeeman splitting lines. In the presence of nanoparticles of different sizes in the sample under study, the Mössbauer spectrum can be a superposition of magnetically split lines and a quadrupole doublet. At the same time, Zeeman lines can be divided into a Zeeman sextet, corresponding to particles with a low relaxation frequency, and a sextet, related to particles whose relaxation frequency is approximately equal to the Larmor frequency of nuclear precession [101]. The Mössbauer spectra of the γ- Fe_2O_3@MIL-88a sample measured at 65 K consist of a Zeeman sextet S1 and doublets D and DS. The S1 sextet corresponds to Fe^{3+} ions in nanoparticles with locked magnetic moments. The DS doublet refers to Fe^{3+} ions in nanoparticles with unlocked magnetic moments. The D doublet is related to Fe^{3+} ions in the structure of the organometallic framework. At a temperature of 55 K, Zeeman splitting lines appear in the spectrum, which corresponds to Fe^{3+} ions in nanoparticles with a relaxation frequency close to the Larmor frequency [102]. To describe these lines, we used the model of multilevel superparamagnetic relaxation [103] implemented in the SpectrRelax program (SR sextet). When carrying out the model interpretation of the spectra, it was assumed that there was no magnetic interaction between the particles. The Mössbauer spectra of the γ- Fe_2O_3@MIL-88a sample measured at temperatures below 55K consist of the D doublet and the S1 and SR sextets. Using the multilevel superparamagnetic relaxation model also made it possible to estimate the parameter $\alpha = (K_{eff}V)/(k_BT)$, where K_{eff} is the magnetic anisotropy, V is the particle volume, and k_B is the Boltzmann constant. At a known value of K_{eff}, this parameter makes it possible to estimate the sizes of nanoparticles. The α sextet parameter of the SR Mössbauer spectra of γ- Fe_2O_3@MIL-88a varies from 0.68 at 55K to 5.8 at 15K. Sextets S1 and SR can correspond to hematite, maghemite, or ferrihydrite nanoparticles. The K_{eff} values for nanoparticles of these compounds, depending on the size, range from $1{\cdot}10^4$ $J{\cdot}sm^{-3}$ to $6{\cdot}10^5$ $J{\cdot}sm^{-3}$ [104–109]. Thus, the sizes of superparamagnetic particles in the γ- Fe_2O_3@MIL-88a sample are distributed in the range from 4 to 10 nm. These data are in good agreement with the results of transmission electron microscopy.

3.6. Photocatalytic experiments

The photocatalytic properties of the synthesized samples were investigated via the reaction of methylene blue (MB) decomposition in hydrogen peroxide water solution. Fig. 11b represents the absorption spectrum of MB. Peaks at 664 and 612 nm correspond to the sulfur-nitrogen conjugated system [17]. The first one is usually attributed to MB monomer, while the shoulder at 612 nm refers to dimer formation [110]. The peak at 290 nm is assigned to the phenothiazine structure [17] (see Fig. S12a).

In general, decolorization of MB solution could result from sorption or catalytic degradation. We performed an experiment to discard the sorption process. Each of the γ-Fe_2O_3@MIL-88a and μMIL-88a samples was mixed with MB solution without an H_2O_2 additive (Table 2, conditions (@-1), (@-2), (μ-1), (μ-2)). However, we did not observe any significant changes (Fig. 11a, Fig. S13b in SI). Thus, the catalytic process was chosen as the main reason for MB degradation.

The intensity of all absorption bands decreased gradually (Fig.11b, Fig. S12a). We observed the peak shift from 664 nm to 656 nm after 50 min of the photocatalytic process (Fig. S12b). It indicates that MB

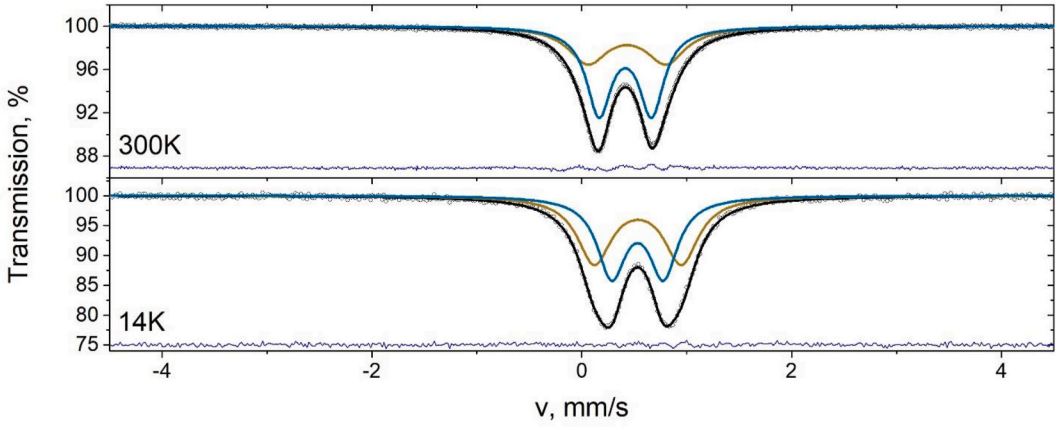

Fig. 9. Mössbauer spectra of MIL-88a sample taken at 300K and 14K. (Points – experimental data, black line – fit, light brown – D1 doublet, light blue – D2 doublet, blue line – the difference between experimental data and fitting).

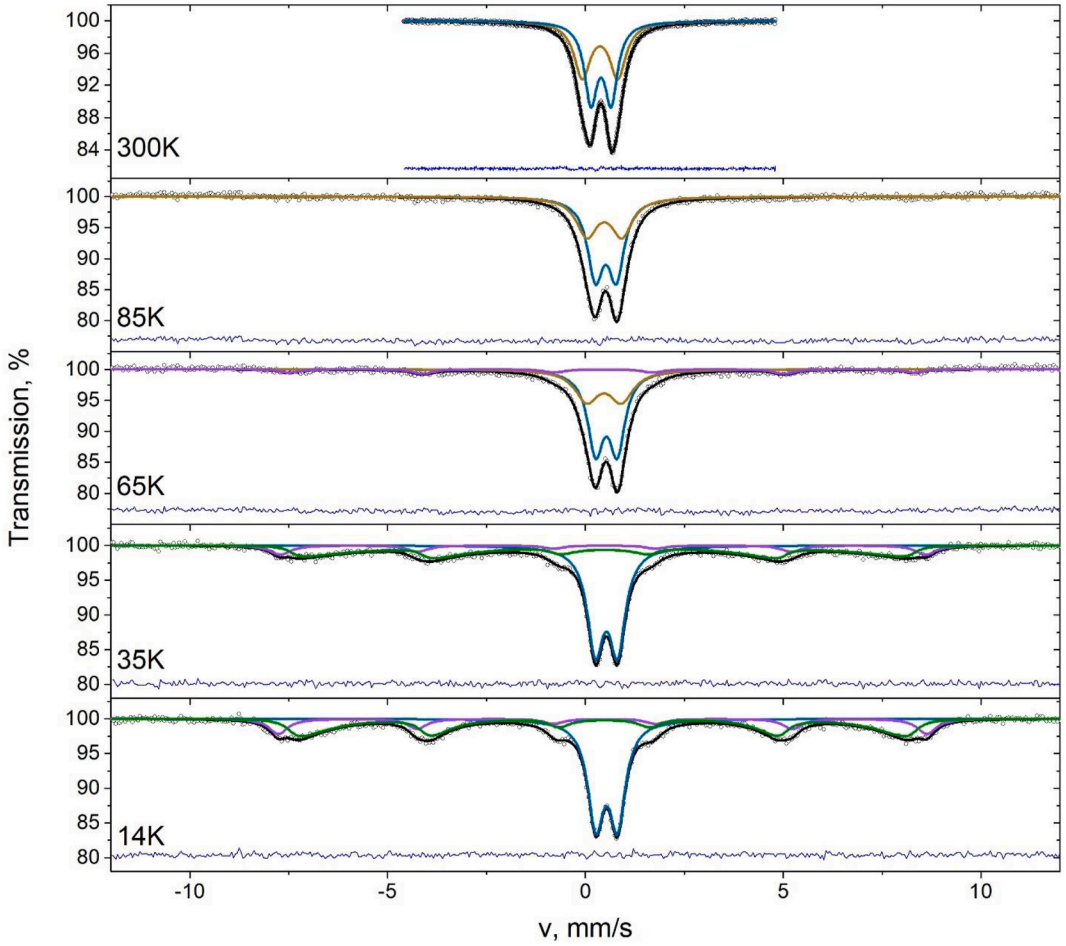

Fig. 10. Mössbauer spectra of γ-Fe_2O_3@MIL-88a sample. (Points – experimental data, black line – fitting, light brown – DS doublet, light blue – D2 doublet, viol line – S1 sextet, green line – MSSR sextet, blue line – difference between experimental data and fitting).

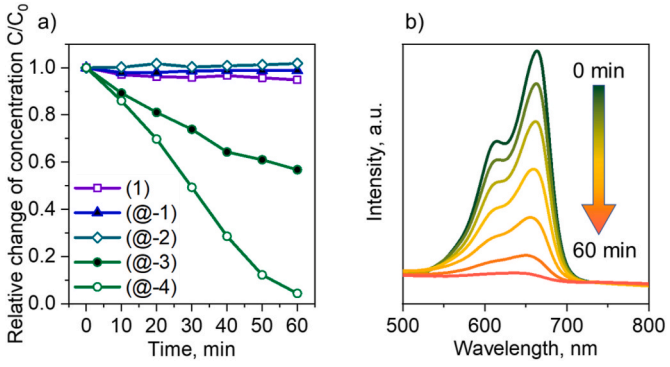

Fig. 11. (a) Catalytic efficiency for the MB degradation as a function of time in systems: (1) MB + H_2O_2 + light, (@-1) MB + γ-Fe_2O_3@MIL-88a, (@-2) MB + γ-Fe_2O_3@MIL-88a + light, (@-3) MB + γ-Fe_2O_3@MIL-88a + H_2O_2, (@-4) MB + γ-Fe_2O_3@MIL-88a + H_2O_2 + light. (b) Successive UV–vis absorption spectra of the MB degradation catalyzed by γ-Fe_2O_3@MIL-88a sample (conditions (@-4)).

decomposition is directed toward the step-wise demethylation pathway of oxidative degradation [111]. The decrease of intensity of all peaks corresponds to the decomposition process. After 60 min absorption spectrum did not contain any new bands confirming the absence of any stable intermediate byproducts. We collected the liquid phase after the catalytic experiment to determine the composition of the products (see SI for details, Fig. S16). According to the FTIR spectrum, the liquid phase after catalysis contained sulfate ions and iron oxide species covered with fumaric acid molecules indicating the partial decomposition of the catalyst. The formation of SO_4^{2-} ions was also prooved by forming white precipitate with $BaCl_2$ solution (Fig. S16b). Thus we conclude that MB was decomposed into inorganic products such as SO_4^{2-}, NO_3^-, CO_2 and H_2O.

As claimed in the introduction part, MIL-88a was applied as the catalyst for Fenton-like processes. Fenton process refers to enhancing H_2O_2 oxidative potential via metallic ions. The original mechanism was first reported in 1894 by Fenton for Fe^{2+} ions [112]. The main steps are flowing [113].

(1) $Fe^{2+} + H_2O_2 \rightarrow Fe^{3+} + \bullet OH + OH^-$
(2) $\bullet OH + H_2O_2 \rightarrow HO_2\bullet + H_2O$
(3) $Fe^{2+} + \bullet OH \rightarrow Fe^{3+} + OH^-$
(4) $Fe^{3+} + HO_2\bullet \rightarrow Fe^{2+} + O_2 + H^+$
(5) $\bullet OH + \bullet OH \rightarrow H_2O_2$

Thus, the first step is the oxidation of Fe^{2+} to Fe^{3+} by H_2O_2 molecules producing •OH-radicals. These radials degrade organic pollutants. Produced Fe^{3+} is reduced in further steps. It provides new Fe^{2+} ions for •OH formation. However, the process results in the accumulation of Fe^{3+} ions in the reaction mixture, which obstructs the further production of hydroxyl radicals. UV-irradiation leads to photochemical regeneration of Fe^{3+} ions. The UV-boosted process is known as the photo-Fenton reaction [114]. It results in the production of more hydroxyl radicals, increasing the rate of organic pollutants degradation. Fe^{3+} regeneration occurs according to the following reactions [113]:

(6) $Fe^{3+} + H_2O_2 + h\nu \rightarrow Fe^{2+} + \bullet OH + H^+$
(7) $Fe^{3+} + H_2O_2 + h\nu \rightarrow Fe^{2+} + HO_2\bullet + H^+$

The μMIL-88a sample demonstrated photocatalytic properties according to the photo-Fenton process (Fig. S15d in SI). Under the light irradiation, the μMIL-88a sample decolorized MB solution in 30 min, while in darkness, no changes were observed even after 1 h of mixing. Thus, H_2O_2 reduced Fe^{3+} in the μMIL-88a sample in the first stage to produce Fe^{2+} and •OH radicals under light irradiation (Eq.6). These radicals destroyed MB molecules.

Unlike the μMIL-88a sample, the γ-Fe_2O_3@MIL-88a composite demonstrated catalytical performance even without light irradiation (Table 2, Fig. S14a in SI). After 1 h, 40% of the MB was converted. We attribute it to the promotional action of γ-Fe_2O_3 nanoparticles. Although the pure γ-Fe_2O_3 sample did not demonstrate any catalytic activity in MB degradation (Fig. S13a), its addition to MIL-88a crystals resulted in the superior performance of the composite in darkness. The Fe^{3+} ions in μMIL-88a and in γ-Fe_2O_3 samples can not be reduced via H_2O_2 without light irradiation. However, in the γ-Fe_2O_3@MIL-88a composite Fe^{3+} ions exhibited catalytic performance without light. We propose that the semiconductor nature of MIL-88a crystals promoted electron transfer, and Fe^{3+} ions on the surface of Fe_2O_3 nanoparticles were able to interact with H_2O_2 producing •OOH and Fe^{2+} ions. Lately, Fe^{2+} ions generated •OH radicals through a reaction with H_2O_2 (Eq. 1). However, the reaction rate was relatively slow due to the low conversion of Fe^{3+} to Fe^{2+} by reacting with H_2O_2. Moreover, the generated •OOH radicals have much lower oxidation potentials than •OH. It led to a lower MB decolorization rate.

Under light irradiation, the γ-Fe_2O_3@MIL-88a sample demonstrated superior photocatalytic performance. MB completely degraded under the light in H_2O_2 with γ-Fe_2O_3@MIL-88a in 1 h. The degradation rate was lower than those of the μMIL-88a sample. We attribute it to the different morphology of MIL-88a crystals. As discussed in the introduction, the rod-like shape of μMIL-88a crystals is preferable for the Fenton-like process [47]. Moreover, sample γ-Fe_2O_3@MIL-88a is composed of MIL-88a crystals and γ-Fe_2O_3 particles. The last ones did not exhibit significant catalytic performance in applied conditions (Fig. S13a). However, these particles initiate the parallel reduction of Fe^{3+} ions. Thus, Fe^{2+} ions are generated from Fe^{3+} ions of the MIL-88a framework via the photo-Fenton process and from Fe^{3+} ions of γ-Fe_2O_3 nanoparticles due to the promotional effect of MIL-88a semiconductor crystal (Fig. 12). Both Fe^{2+} ions interact with H_2O_2 providing •OH radicals for MB degradation.

Moreover, the γ-Fe_2O_3@MIL-88a sample provides essential benefits in actual application due to magnetic properties for collecting a heterogeneous catalyst via a magnetic field for reuse. We investigated recycling options for the γ-Fe_2O_3@MIL-88a catalyst (see details in SI, part 6). It was shown that the material is stable in two cycles while starting from the third one, its effectiveness was reduced four times. The XRD powder patterns, FTIR spectra, and TGA of the catalyst after the third cycle showed significant degradation of its structure (Fig. S17). The MIL-88a component was decomposed due to the acidic medium of the reaction mixture, which was estimated at 4.6 after 10 min of the experiment and was decreased to 4.0 after 1 h. The protective shell was reported to increase the stability of MIL-88a catalysts in the acidic medium [48].

4. Conclusions

This work presents a new one-step electrochemical synthesis of nanosized γ-Fe_2O_3@MIL-88a magnetic composite. Unlike other methods for preparing MIL-88a and composites, it does not require special and/or extreme conditions. Composite was obtained at room temperature and for a short time. Moreover, the synthesis did not require hazardous or toxic reagents. The γ-Fe_2O_3@MIL-88a sample comprised diamond-like MIL-88a nanocrystals and magnetic Fe_2O_3 particles. The electrochemical synthesis was interpreted as a multistep process. In the first stage, iron oxide species were formed in the reaction mixture as a result of Fe-anode dissolution. Later, part of these clusters acted as nuclei for MIL-88a growth, resulting in diamond-shaped MOF nanoparticles. It should be noted that due to crystal growth features, the synthesis of diamond-like MIL-88a nanoparticles without DMF is a challenging task. The other part of the iron oxide species grew and formed magnetic γ-Fe_2O_3 nanoparticles. Thus, the proposed electrochemical technique allowed us to obtain a composite of MIL-88a diamond-like nanocrystals with magnetic nanoparticles on their surface as a one-pot room-temperature process.

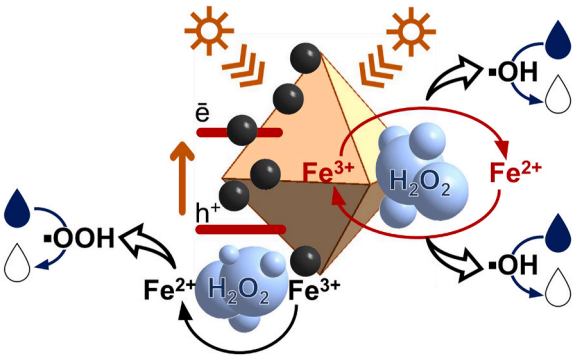

Fig. 12. Scheme of the photocatalytic process of MB degradation using γ-Fe_2O_3@MIL-88a sample.

Using careful analysis of XANES and Mössbauer spectra and XRD patterns, we proved that magnetic nanoparticles are γ-Fe_2O_3. Obtained composite possessed magnetic properties and could be separated from the reaction mixture via a permanent magnet.

We applied obtained composite for photo-Fenton degradation of MB in the presence of H_2O_2. Magnetic γ-Fe_2O_3 nanoparticles promoted the catalytic properties of the obtained material. Even without light irradiation, γ-Fe_2O_3@MIL-88a composite converted 40% of MB in an hour. Neither pure γ-Fe_2O_3 nor rod-shaped MIL-88a did not show any effect on MB solution without light. Moreover, γ-Fe_2O_3 particles provided a magnetic response to composite. It gives a great advantage to heterogeneous catalysts. Obtained composite can be collected from the reaction mixture via a permanent magnet for further recycling. We suppose that provided here, a one-pot electrochemical synthesis of magnetic composite for photo-Fenton dye degradation could be used for wastewater treatment.

Declaration of competing interest

The authors declare that they have no known competing financial interests or personal relationships that could have appeared to influence the work reported in this paper.

Acknowledgements

This work was supported by Russian Science Foundation (Project No. 19-73-10069).

The research was carried out using the scientific equipment of the Center for Collective Use “Nanoscale structure of matter."

The authors thank the Kurchatov Synchrotron Radiation Source for the beamtime allocation.

Appendix A. Supplementary data

Supplementary data to this article can be found online at https://doi.org/10.1016/j.ceramint.2022.08.076.

References

[1] J.L.C. Rowsell, O.M. Yaghi, Metal-organic frameworks: a new class of porous materials, Microporous and Mesoporous Materials 73 (2004) 3–14, https://doi.org/10.1016/j.micromeso.2004.03.034.

[2] M.J. Rosseinsky, Recent developments in metal-organic framework chemistry: design, discovery, permanent porosity and flexibility, Microporous and Mesoporous Materials 73 (2004) 15–30, https://doi.org/10.1016/j.micromeso.2003.05.001.

[3] M.A. Agafonov, E.V. Alexandrov, N.A. Artyukhova, G.E. Bekmukhamedov, V. A. Blatov, V.V. Butova, Y.M. Gayfulin, A.A. Garibyan, Z.N. Gafurov, Y. G. Gorbunova, et al., Metal-organic frameworks in Russia: from the synthesis and structure to functional properties and materials, Journal of Structural Chemistry 63 (2022) 671–843, https://doi.org/10.1134/S0022476622050018.

[4] D.J.L. Tranchemontagne, Z. Ni, M. O'Keeffe, O.M. Yaghi, Reticular chemistry of metal-organic polyhedra, Angewandte Chemie-International Edition 47 (2008) 5136–5147, https://doi.org/10.1002/anie.200705008.

[5] V.V. Butova, M.A. Soldatov, A.A. Guda, K.A. Lomachenko, C. Lamberti, Metal-organic frameworks: structure, properties, methods of synthesis and characterization, Russian Chemical Reviews 85 (2016) 280–307, https://doi.org/10.1070/rcr4554.

[6] V.A. Polyakov, V.V. Butova, E.A. Erofeeva, A.A. Tereshchenko, A.V. Soldatov, MW Synthesis of ZIF-7. The effect of solvent on particle size and hydrogen sorption properties, Energies 13 (2020) 6306, https://doi.org/10.3390/en13236306.

[7] V.V. Butova, I.A. Pankin, O.A. Burachevskaya, K.S. Vetlitsyna-Novikova, A. V. Soldatov, New fast synthesis of MOF-801 for water and hydrogen storage: modulator effect and recycling options, Inorg. Chim. Acta 514 (2021), 120025, https://doi.org/10.1016/j.ica.2020.120025.

[8] V.V. Butova, O.A. Burachevskaya, V.A. Podshibyakin, E.N. Shepelenko, A. A. Tereshchenko, S.O. Shapovalova, O.I. Il'in, V.A. Bren', A.V. Soldatov, Photoswitchable zirconium mof for light-driven hydrogen storage, Polym 13 (2021) 4052, https://doi.org/10.3390/polym13224052.

[9] Z. Chen, K.O. Kirlikovali, K.B. Idrees, M.C. Wasson, O.K. Farha, Porous materials for hydrogen storage, Chem 8 (2022) 693–716, https://doi.org/10.1016/j.chempr.2022.01.012.

[10] Y. Li, Y. Wang, W. Fan, D. Sun, Flexible metal-organic frameworks for gas storage and separation, Dalton Transactions 51 (2022) 4608–4618, https://doi.org/10.1039/d1dt03842g.

[11] S. Rojas, A. Arenas-Vivo, P. Horcajada, Metal-organic frameworks: a novel platform for combined advanced therapies, Coordination Chemistry Reviews 388 (2019) 202–226, https://doi.org/10.1016/j.ccr.2019.02.032.

[12] D.B. Trushina, A.Y. Sapach, O.A. Burachevskaia, P.V. Medvedev, D.N. Khmelenin, T.N. Borodina, M.A. Soldatov, V.V. Butova, Doxorubicin-Loaded core–shell UiO-66@SiO2 metal–organic frameworks for targeted cellular uptake and cancer treatment, Pharmaceutics 14 (2022) 1325, https://doi.org/10.3390/pharmaceutics14071325.

[13] I.E. Gorban, M.A. Soldatov, V.V. Butova, P.V. Medvedev, O.A. Burachevskaya, A. Belanova, P. Zolotukhin, A.V. Soldatov, L-leucine loading and release in MIL-100 nanoparticles, Int. J. Mol. Sci. 21 (2020), https://doi.org/10.3390/ijms21249758, 9758-11.

[14] V.V. Butova, O.A. Burachevskaya, M.A. Muratidi, I.I. Surzhikova, P.V. Zolotukhin, P.V. Medvedev, I.E. Gorban, A.A. Kuzharov, M.A. Soldatov, Loading of the model amino acid leucine in UiO-66 and UiO-66-NH2: optimization of metal-organic framework carriers and evaluation of host-guest interactions, Inorg. Chem. 60 (2021) 5694–5703, https://doi.org/10.1021/acs.inorgchem.0c03751.

[15] C.H. Wang, P. Cheng, Y.Y. Yao, Y. Yamauchi, X. Yan, J.S. Li, J. Na, In-situ fabrication of nanoarchitectured MOF filter for water purification, Journal of hazardous materials 392 (2020), 122164, https://doi.org/10.1016/j.jhazmat.2020.122164.

[16] V.V. Butova, V.A. Polyakov, E.A. Erofeeva, I.S. Yahia, H.Y. Zahran, A.F. Abd El-Rehim, A.M. Aboraia, A.V. Soldatov, Modification of ZIF-8 with triethylamine molecules for enhanced iodine and bromine adsorption, Inorg. Chim. Acta 509 (2020), 119678, https://doi.org/10.1016/j.ica.2020.119678.

[17] V.V. Butova, A.M. Aboraia, M. Solayman, I.S. Yahia, H.Y. Zahran, A.F. Abd El-Rehim, H. Algarni, G. Khabiri, A.V. Soldatov, The joint effect of naphthalene-system and defects on dye removal by UiO-66 derivatives, Microporous and Mesoporous Materials 325 (2021), 111314, https://doi.org/10.1016/j.micromeso.2021.111314.

[18] H. Daglar, C. Altintas, I. Erucar, G. Heidari, E.N. Zare, O. Moradi, V. Srivastava, S. Iftekhar, S. Keskin, M. Sillanpää, Metal-organic framework-based materials for the abatement of air pollution and decontamination of wastewater, Chemosphere 303 (2022), 135082, https://doi.org/10.1016/j.chemosphere.2022.135082.

[19] C. Xia, C.Y. Yu, M.M. Cao, J.F. Xia, D.Y. Jiang, G.H. Zhou, D.F. Zhang, H.L. Li, A Eu and Tb co-doped MOF-5 compound for ratiometric high temperature sensing, Ceramics International 44 (2018) 21040–21046, https://doi.org/10.1016/j.ceramint.2018.08.140.

[20] R. Zhang, L. Lu, Y. Chang, M. Liu, Gas sensing based on metal-organic frameworks: concepts, functions, and developments, Journal of hazardous materials 429 (2022), 128321, https://doi.org/10.1016/j.jhazmat.2022.128321.

[21] T. Deng, X.L. Men, X.C. Jiao, J. Wang, CNTs decorated Cu-BTC with catalytic effect for high-stability lithium-sulfur batteries, Ceramics International 48 (2022) 4352–4360, https://doi.org/10.1016/j.ceramint.2021.10.230.

[22] F. Zhang, J.J. Ma, H. Yao, Ultrathin Ni-MOF nanosheet coated NiCo2O4 nanowire arrays as a high-performance binder-free electrode for flexible hybrid supercapacitors, Ceramics International 45 (2019) 24279–24287, https://doi.org/10.1016/j.ceramint.2019.08.140.

[23] Y. Zhang, Q. Huang, J. Liu, J.E. Zhou, X. Lin, A. Zeb, R.C.K. Reddy, X. Xu, Recent advances in Fe-based metal-organic framework derivatives for battery applications, Sustain. Energy Fuels 6 (2022) 2665–2691, https://doi.org/10.1039/d2se00319h.

[24] D. Farrusseng, S. Aguado, C. Pinel, Metal-organic frameworks: opportunities for catalysis, Angewandte Chemie-International Edition 48 (2009) 7502–7513, https://doi.org/10.1002/anie.200806063.

[25] S.B. Wang, X.C. Wang, Multifunctional metal-organic frameworks for photocatalysis, Small 11 (2015) 3097–3112, https://doi.org/10.1002/smll.201500084.

[26] S. Peng, M. Li, X.X. Yang, P.H. Li, H. Liu, W. Xiong, X.Y. Peng, Atomic layer deposition of Pt nanoparticles on ZrO2 based metal-organic frameworks for increased photocatalytic activity, Ceramics International 45 (2019) 18128–18134, https://doi.org/10.1016/j.ceramint.2019.05.306.

[27] R. Yan, Y. Zhao, H. Yang, X.J. Kang, C. Wang, L.L. Wen, Z.D. Lu, Ultrasmall Au nanoparticles embedded in 2D mixed-ligand metal-organic framework nanosheets exhibiting highly efficient and size-selective catalysis, Advanced Functional Materials 28 (2018), 1802021, https://doi.org/10.1002/adfm.201802021.

[28] H.M. He, Q.Q. Zhu, Y. Yan, H.W. Zhang, Z.Y. Han, H.M. Sun, J. Chen, C.P. Li, Z. H. Zhang, M. Du, Metal-organic framework supported Au nanoparticles with organosilicon coating for high-efficiency electrocatalytic N2 reduction to NH3, Applied Catalysis B-Environmental 302 (2022), 120840, https://doi.org/10.1016/j.apcatb.2021.120840.

[29] K. Matsuyama, M. Motomura, T. Kato, T. Okuyama, H. Muto, Catalytically active Pt nanoparticles immobilized inside the pores of metal organic framework using supercritical CO2 solutions, Microporous and Mesoporous Materials 225 (2016) 26–32, https://doi.org/10.1016/j.micromeso.2015.12.005.

[30] A.A. Tereshchenko, V.V. Butova, A.A. Guda, O.A. Burachevskaya, A.L. Bugaev, A. N. Bulgakov, A.A. Skorynina, Y.V. Rusalev, I.V. Pankov, V.A. Volochaev, et al., Rational functionalization of UiO-66 with Pd nanoparticles: synthesis and in situ fourier-transform infrared monitoring, Inorg. Chem. (2022), https://doi.org/10.1021/acs.inorgchem.1c03340.

[31] E.G. Kamyshova, A.A. Skorynina, A.L. Bugaev, C. Lamberti, A.V. Soldatov, Formation and growth of Pd nanoparticles in UiO-67 MOF by in situ EXAFS, Radiat. Phys. Chem. 175 (2020), 108144, https://doi.org/10.1016/j.radphyschem.2019.02.003.

[32] J. Vercammen, M. Bocus, S. Neale, A. Bugaev, P. Tomkins, J. Hajek, S. Van Minnebruggen, A. Soldatov, A. Krajnc, G. Mali, et al., Shape-selective C–H activation of aromatics to biarylic compounds using molecular palladium in zeolites, Nat. Catal. 3 (2020) 1002–1009, https://doi.org/10.1038/s41929-020-00533-6.

[33] D.Y. Hong, Y.K. Hwang, C. Serre, G. Ferey, J.S. Chang, Porous chromium terephthalate MIL-101 with coordinatively unsaturated sites: surface functionalization, encapsulation, sorption and catalysis, Advanced Functional Materials 19 (2009) 1537–1552, https://doi.org/10.1002/adfm.200801130.

[34] C. Serre, C. Mellot-Draznieks, S. Surble, N. Audebrand, Y. Filinchuk, G. Ferey, Role of solvent-host interactions that lead to very large swelling of hybrid frameworks, Science 315 (2007) 1828–1831, https://doi.org/10.1126/science.1137975.

[35] N.A. Ramsahye, T.K. Trung, L. Scott, F. Nouar, T. Devic, P. Horcajada, E. Magnier, O. David, C. Serre, P. Trens, Impact of the flexible character of MIL-88 iron(III) dicarboxylates on the adsorption of n-alkanes, Chemistry of Materials 25 (2013) 479–488, https://doi.org/10.1021/cm303830b.

[36] T. Chalati, P. Horcajada, R. Gref, P. Couvreur, C. Serre, Optimisation of the synthesis of MOF nanoparticles made of flexible porous iron fumarate MIL-88A, Journal of Materials Chemistry 21 (2011) 2220–2227, https://doi.org/10.1039/C0JM03563G.

[37] C. Mellot-Draznieks, C. Serre, S. Surble, N. Audebrand, G. Ferey, Very large swelling in hybrid frameworks: a combined computational and powder diffraction study, Journal of the American Chemical Society 127 (2005) 16273–16278, https://doi.org/10.1021/ja054900x.

[38] R. Liang, F. Jing, L. Shen, N. Qin, L. Wu, MIL-53(Fe) as a highly efficient bifunctional photocatalyst for the simultaneous reduction of Cr(VI) and oxidation of dyes, Journal of hazardous materials 287 (2015) 364–372, https://doi.org/10.1016/j.jhazmat.2015.01.048.

[39] N. Liu, J. Wu, F. Fei, J. Lei, W. Shi, G. Quan, S. Zeng, X. Zhang, L. Tang, Ibuprofen degradation by a synergism of facet-controlled MIL-88B(Fe) and persulfate under simulated visible light, Journal of Colloid and Interface Science 612 (2022) 1–12, https://doi.org/10.1016/j.jcis.2021.12.142.

[40] X. Zhang, K. Yue, R. Rao, J. Chen, Q. Liu, Y. Yang, F. Bi, Y. Wang, J. Xu, N. Liu, Synthesis of acidic MIL-125 from plastic waste: significant contribution of N orbital for efficient photocatalytic degradation of chlorobenzene and toluene, Applied Catalysis B: Environmental 310 (2022), 121300, https://doi.org/10.1016/j.apcatb.2022.121300.

[41] D. Wang, F. Jia, H. Wang, F. Chen, Y. Fang, W. Dong, G. Zeng, X. Li, Q. Yang, X. Yuan, Simultaneously efficient adsorption and photocatalytic degradation of tetracycline by Fe-based MOFs, Journal of Colloid and Interface Science 519 (2018) 273–284, https://doi.org/10.1016/j.jcis.2018.02.067.

[42] C.-E. Tan, E.-C. Su, M.-Y. Wey, Development of physicochemically stable Z-scheme MIL-88A/g-C3N4 heterojunction photocatalyst with excellent charge transfer for improving acid red 1 dye decomposition efficiency, Applied Surface Science 590 (2022), 152954, https://doi.org/10.1016/j.apsusc.2022.152954.

[43] J. Gu, Q. Li, X. Long, X. Zhou, N. Liu, Z. Li, Fabrication of magnetic dual Z-scheme heterojunction materials for efficient photocatalytic performance: the study of ternary novel MIL-88A(Fe)/BiOBr/SrFe12O19 nanocomposite, Separation and Purification Technology 289 (2022), 120778, https://doi.org/10.1016/j.seppur.2022.120778.

[44] D. Roy, S. Neogi, S. De, Mechanistic investigation of photocatalytic degradation of Bisphenol-A using MIL-88A(Fe)/MoS2 Z-scheme heterojunction composite assisted peroxymonosulfate activation, Chemical Engineering Journal 428 (2022), 131028, https://doi.org/10.1016/j.cej.2021.131028.

[45] S. Jiang, Z. Zhao, J. Chen, Y. Yang, C. Ding, Y. Yang, Y. Wang, N. Liu, L. Wang, X. Zhang, Recent research progress and challenges of MIL-88(Fe) from synthesis to advanced oxidation process, Surfaces and Interfaces 30 (2022), 101843, https://doi.org/10.1016/j.surfin.2022.101843.

[46] W.X. Huang, W.M. Liu, Z.Z. Yang, Y.Y. Chen, G.B. Li, X.Y. Liao, MIL-88A anchoring on different morphological g-C3N4 for enhanced Fenton performance, Microporous and Mesoporous Materials 329 (2022), 111531, https://doi.org/10.1016/j.micromeso.2021.111531.

[47] X. Liao, F. Wang, F. Wang, Y. Cai, Y. Yao, B.-T. Teng, Q. Hao, L. Shuxiang, Synthesis of (100) surface oriented MIL-88A-Fe with rod-like structure and its enhanced fenton-like performance for phenol removal, Applied Catalysis B: Environmental 259 (2019), 118064, https://doi.org/10.1016/j.apcatb.2019.118064.

[48] W. Huang, H. Shao, M. Song, Z. Yang, G. Li, X. Liao, Perylene diimides coated Fe-MOFs as acid-tolerant photo-Fenton catalyst for phenol removal, Applied Surface Science 547 (2021), 149222, https://doi.org/10.1016/j.apsusc.2021.149222.

[49] D.D. Chen, X.H. Yi, L. Ling, C.C. Wang, P. Wang, Photocatalytic Cr(VI) sequestration and photo-Fenton bisphenol A decomposition over white light responsive PANI/MIL-88A(Fe), Applied Organometallic Chemistry 34 (2020), e5795, https://doi.org/10.1002/aoc.5795.

[50] H.F. Fu, X.X. Song, L. Wu, C. Zhao, P. Wang, C.C. Wang, Room-temperature preparation of MIL-88A as a heterogeneous photo-Fenton catalyst for degradation of rhodamine B and bisphenol a under visible light, Materials Research Bulletin 125 (2020), 110806, https://doi.org/10.1016/j.materresbull.2020.110806.

[51] Z.F. Yang, X.N. Xia, L.H. Shao, L.L. Wang, Y.T. Liu, Efficient photocatalytic degradation of tetracycline under visible light by Z-scheme Ag3PO4/mixed-valence MIL-88A(Fe) heterojunctions: mechanism insight, degradation pathways and DFT calculation, Chemical Engineering Journal 410 (2021), 128454, https://doi.org/10.1016/j.cej.2021.128454.

[52] H. Liu, H. Yin, M. Zhu, Z. Dang, Degradation of organophosphorus flame retardants in heterogeneous photo-Fenton system driven by Fe(III)-based metal organic framework: intermediates and their potential interference on bacterial metabolism, Chemosphere 291 (2022), 133072, https://doi.org/10.1016/j.chemosphere.2021.133072.

[53] D. Yu, L. Wang, T. Yang, G. Yang, D. Wang, H. Ni, M. Wu, Tuning Lewis acidity of iron-based metal-organic frameworks for enhanced catalytic ozonation, Chemical Engineering Journal 404 (2021), 127075, https://doi.org/10.1016/j.cej.2020.127075.

[54] G. Ren, K. Zhao, L. Zhao, A Fenton-like method using ZnO doped MIL-88A for degradation of methylene blue dyes, RSC Advances 10 (2020) 39973–39980, https://doi.org/10.1039/D0RA08076D.

[55] R. Yue, B. Raisi, J. Rahmatinejad, Z. Ye, B. Barbeau, M.S. Rahaman, A photo-Fenton nanocomposite ultrafiltration membrane for enhanced dye removal with self-cleaning properties, Journal of Colloid and Interface Science 604 (2021) 458–468, https://doi.org/10.1016/j.jcis.2021.06.157.

[56] K.-Y. Andrew Lin, F.-K. Hsu, Magnetic iron/carbon nanorods derived from a metal organic framework as an efficient heterogeneous catalyst for the chemical oxidation process in water, RSC Advances 5 (2015) 50790–50800, https://doi.org/10.1039/C5RA06043E.

[57] A. Xie, J. Cui, J. Yang, Y. Chen, J. Lang, C. Li, Y. Yan, J. Dai, Graphene oxide/Fe (III)-based metal-organic framework membrane for enhanced water purification based on synergistic separation and photo-Fenton processes, Applied Catalysis B: Environmental 264 (2020), 118548, https://doi.org/10.1016/j.apcatb.2019.118548.

[58] L. Zhang, Y. He, P. Luo, L. Ma, S. Li, Y. Nie, F. Zhong, Y. Wang, L. Chen, Photocatalytic GO/M88A “interceptor plate” assembled nanofibrous membrane with photo-Fenton self-cleaning performance for oil/water emulsion separation, Chemical Engineering Journal 427 (2022), 130948, https://doi.org/10.1016/j.cej.2021.130948.

[59] E. Bagherzadeh, S.M. Zebarjad, H.R. Madaah Hosseini, P. Chagnon, Preparation, optimization and evolution of the kinetic mechanism of an Fe-MIL-88A metal–organic framework, CrystEngComm 21 (2019) 544–553, https://doi.org/10.1039/C8CE01876F.

[60] L. Wang, Y.Y. Zhang, X. Li, Y.Z. Xie, J. He, J. Yu, Y.H. Song, The MIL-88a-derived Fe3O4-carbon hierarchical nanocomposites for electrochemical sensing, Scientific Reports 5 (2015), 14341, https://doi.org/10.1038/srep14341.

[61] L. Wang, J. Yu, X.T. Dong, X. Li, Y.Z. Xie, S.H. Chen, P. Li, H.Q. Hou, Y.H. Song, Three-dimensional macroporous carbon/Fe3O4-doped porous carbon nanorods for high-performance supercapacitor, Acs Sustainable Chemistry & Engineering 4 (2016) 1531–1537, https://doi.org/10.1021/acssuschemeng.5b01474.

[62] Y. Wang, X.M. Guo, Z.K. Wang, M.F. Lu, B. Wu, Y. Wang, C. Yan, A.H. Yuan, H. X. Yang, Controlled pyrolysis of MIL-88A to Fe2O3@C nanocomposites with varied morphologies and phases for advanced lithium storage, Journal of Materials Chemistry A 5 (2017) 25562–25573, https://doi.org/10.1039/c7ta08314a.

[63] X.J. Li, F.Z. Liao, L.M. Ye, L.Z. Yeh, Controlled pyrolysis of MIL-88A to prepare iron/carbon composites for synergistic persulfate oxidation of phenol: catalytic performance and mechanism, Journal of hazardous materials 398 (2020), 122938, https://doi.org/10.1016/j.jhazmat.2020.122938.

[64] V.V. Butova, A.M. Aboraia, V.V. Shapovalov, N.A. Dzhangiryan, E. D. Papkovskaya, O.I. Ilin, S.P. Kubrin, A.A. Guda, A.V. Soldatov, Iron (II) fluoride cathode material derived from MIL-88A, J Alloys Compd 916 (2022), 165438, https://doi.org/10.1016/j.jallcom.2022.165438.

[65] Y. Liu, Y. Huang, A. Xiao, H. Qiu, L. Liu, Preparation of magnetic Fe3O4/MIL-88a nanocomposite and its adsorption properties for Bromophenol blue dye in aqueous solution, Nanomaterials 9 (2019), https://doi.org/10.3390/nano9010051.

[66] X. Zhang, Q. Xia, Y. Zhou, Y. Wang, Z. Jiang, Z. Yao, High-activity and excellent-reusability γ-Fe2O3/SiO2 coating on TC4 titanium alloy by plasma electrolytic oxidation for enhanced photo-Fenton degradation, Chemosphere 303 (2022), 135105, https://doi.org/10.1016/j.chemosphere.2022.135105.

[67] M. Moztahida, J. Jang, M. Nawaz, S.-R. Lim, D.S. Lee, Effect of rGO loading on Fe3O4: a visible light assisted catalyst material for carbamazepine degradation, Science of The Total Environment 667 (2019) 741–750, https://doi.org/10.1016/j.scitotenv.2019.02.376.

[68] O. Akhavan, R. Azimirad, Photocatalytic property of Fe2O3 nanograin chains coated by TiO2 nanolayer in visible light irradiation, Applied Catalysis A: General 369 (2009) 77–82, https://doi.org/10.1016/j.apcata.2009.09.001.

[69] S. Guo, G. Zhang, Y. Guo, J.C. Yu, Graphene oxide–Fe2O3 hybrid material as highly efficient heterogeneous catalyst for degradation of organic contaminants, Carbon 60 (2013) 437–444, https://doi.org/10.1016/j.carbon.2013.04.058.

[70] J.H. Chu, J.K. Kang, S.J. Park, C.G. Lee, Enhanced sonocatalytic degradation of bisphenol A with a magnetically recoverable biochar composite using rice husk and rice bran as substrate, Journal of Environmental Chemical Engineering 9 (2021), 105284, https://doi.org/10.1016/j.jece.2021.105284.

[71] N. Ferroudj, J. Nzimoto, A. Davidson, D. Talbot, E. Briot, V. Dupuis, A. Bée, M. S. Medjram, S. Abramson, Maghemite nanoparticles and maghemite/silica nanocomposite microspheres as magnetic Fenton catalysts for the removal of water pollutants, Applied Catalysis B: Environmental 136–137 (2013) 9–18, https://doi.org/10.1016/j.apcatb.2013.01.046.

[72] F. Family, Electrochemical synthesis and processing of materials: from fractal electrodes to epitaxial thin films, in: Proceedings of the Symposium on Electrochemical Synthesis and Modification of Materials, at the 1996, MRS Fall Meeting, Boston, Ma, 1996, pp. 123–140. Dec 02-05.

[73] A. Ghoorchian, A. Afkhami, T. Madrakian, M. Ahmadi, Chapter 9 - electrochemical synthesis of MOFs, in: M. Mozafari (Ed.), Metal-Organic Frameworks for Biomedical Applications, Woodhead Publishing, 2020, pp. 177–195.

[74] M.V. Varsha, G. Nageswaran, Review-direct electrochemical synthesis of metal organic frameworks, Journal of the Electrochemical Society 167 (2020), 155527, https://doi.org/10.1149/1945-7111/abc6c6.

[75] N. Campagnol, T. Van Assche, T. Boudewijns, J. Denayer, K. Binnemans, D. De Vos, J. Fransaer, High pressure, high temperature electrochemical synthesis of metal–organic frameworks: films of MIL-100 (Fe) and HKUST-1 in different morphologies, Journal of Materials Chemistry A 1 (2013) 5827–5830, https://doi.org/10.1039/C3TA10419B.

[76] F. Mokhtarian, B. Rastegari, S. Zeinali, M. Tohidi, H.R. Karbalaei-Heidari, Theranostic effect of folic acid functionalized MIL-100(Fe) for delivery of prodigiosin and simultaneous tracking-combating breast cancer, Journal of Nanomaterials 2022 (2022), 1108865, https://doi.org/10.1155/2022/1108865.

[77] W. Wu, G.E. Decker, A.E. Weaver, A.I. Arnoff, E.D. Bloch, J. Rosenthal, Facile and rapid room-temperature electrosynthesis and controlled surface growth of Fe-MIL-101 and Fe-MIL-101-NH2, ACS Central Science 7 (2021) 1427–1433, https://doi.org/10.1021/acscentsci.1c00686.

[78] J. Rodriguez-Carvajal, Recent advances in magnetic structure determination by neutron powder diffraction, Physica B: Condensed Matter 192 (1993) 55–69, https://doi.org/10.1016/0921-4526(93)90108-I.

[79] A.A. Chernyshov, A.A. Veligzhanin, Y.V. Zubavichus, Structural materials science end-station at the Kurchatov synchrotron radiation source: recent instrumentation upgrades and experimental results, Nucl. Instrum. Methods Phys. Res. Sect. A-Accel. Spectrom. Dect. Assoc. Equip. 603 (2009) 95–98, https://doi.org/10.1016/j.nima.2008.12.167.

[80] B. Ravel, M.A. Newville, H. Artemis, Data analysis for X-ray absorption spectroscopy using IFEFFIT, J. Synchrot. Radiat. 12 (2005) 537–541, https://doi.org/10.1107/s0909049505012719.

[81] M.E. Matsnev, V.S. SpectrRelax Rusakov, An application for Mössbauer spectra modeling and fitting, AIP Conference Proceedings 1489 (2012) 178–185, https://doi.org/10.1063/1.4759488.

[82] C. Serre, F. Millange, S. Surblé, G. Férey, A route to the synthesis of trivalent transition-metal porous carboxylates with trimeric secondary building units, Angewandte Chemie International Edition 43 (2004) 6285–6289, https://doi.org/10.1002/anie.200454250.

[83] V.P. Viswanathan, S.V. Mathew, D.P. Dubal, N.N. Adarsh, S. Mathew, Exploring the effect of morphologies of Fe(III) metal-organic framework MIL-88a(Fe) on the photocatalytic degradation of rhodamine B, ChemistrySelect 5 (2020) 7534–7542, https://doi.org/10.1002/slct.202001670.

[84] P. Hirschle, C. Hirschle, K. Boll, M. Doblinger, M. Hohn, J.M. Tuffnell, C. W. Ashling, D.A. Keen, T.D. Bennett, J.O. Radler, et al., Tuning the morphological appearance of iron(III) fumarate: impact on material characteristics and biocompatibility, Chemistry of Materials 32 (2020) 2253–2263, https://doi.org/10.1021/acs.chemmater.9b03662.

[85] M.E. Mahmoud, M.F. Amira, S.M. Seleim, A.K. Mohamed, Amino-decorated magnetic metal-organic framework as a potential novel platform for selective

removal of chromium (Vl), cadmium (II) and lead (II), Journal of hazardous materials 381 (2020), 120979, https://doi.org/10.1016/j.jhazmat.2019.120979.
[86] S.W. Hwang, A. Umar, G.N. Dar, S.H. Kim, R.I. Badran, Synthesis and characterization of iron oxide nanoparticles for phenyl hydrazine sensor applications, Sensor Letters 12 (2014) 97–101, https://doi.org/10.1166/sl.2014.3224.
[87] N. Liu, W. Huang, X. Zhang, L. Tang, L. Wang, Y. Wang, M. Wu, Ultrathin graphene oxide encapsulated in uniform MIL-88A(Fe) for enhanced visible light-driven photodegradation of RhB, Applied Catalysis B: Environmental 221 (2018) 119–128, https://doi.org/10.1016/j.apcatb.2017.09.020.
[88] K.-Y. Andrew Lin, H.-A. Chang, C.-J. Hsu, Iron-based metal organic framework, MIL-88A, as a heterogeneous persulfate catalyst for decolorization of Rhodamine B in water, RSC Advances 5 (2015) 32520–32530, https://doi.org/10.1039/C5RA01447F.
[89] J. Tang, J. Wang, Metal organic framework with coordinatively unsaturated sites as efficient fenton-like catalyst for enhanced degradation of sulfamethazine, Environmental Science & Technology 52 (2018) 5367–5377, https://doi.org/10.1021/acs.est.8b00092.
[90] Y.W. Gao, S.M. Li, Y.X. Li, L.Y. Yao, H. Zhang, Accelerated photocatalytic degradation of organic pollutant over metal-organic framework MIL-53(Fe) under visible LED light mediated by persulfate, Applied Catalysis B-Environmental 202 (2017) 165–174, https://doi.org/10.1016/j.apcatb.2016.09.005.
[91] C. Cheng, J. Li, Y. Wen, J. Wang, C. Jin, C. Sun, H. Wang, H. Wei, X. Yang, Deactivation mechanism of Fe/Al2O3 catalyst during the ozonation of reverse osmosis concentrates (ROCs): effect of silicate, Chemical Engineering Journal Advances 1 (2020), 100003, https://doi.org/10.1016/j.ceja.2020.100003.
[92] T.S. Alomar, N. AlMasoud, M.A. Awad, M.F. El-Tohamy, D.A. Soliman, An eco-friendly plant-mediated synthesis of silver nanoparticles: characterization, pharmaceutical and biomedical applications, Materials Chemistry and Physics 249 (2020), 123007, https://doi.org/10.1016/j.matchemphys.2020.123007.
[93] W.Y. Huang, C.W. Jing, X.D. Zhang, M.Q. Tang, L. Tang, M.H. Wu, N. Liu, Integration of plasmonic effect into spindle-shaped MIL-88A(Fe): steering charge flow for enhanced visible-light photocatalytic degradation of ibuprofen, Chemical Engineering Journal 349 (2018) 603–612, https://doi.org/10.1016/j.cej.2018.05.121.
[94] J. Amaro-Gahete, R. Klee, D. Esquivel, J.R. Ruiz, C. Jimenez-Sanchidrian, F. J. Romero-Salguero, Fast ultrasound-assisted synthesis of highly crystalline MIL-88A particles and their application as ethylene adsorbents, Ultrason. Sonochem. 50 (2019) 59–66, https://doi.org/10.1016/j.ultsonch.2018.08.027.
[95] M.D. Mukadam, S.M. Yusuf, P. Sharma, S.K. Kulshreshtha, Particle size-dependent magnetic properties of γ-Fe2O3 nanoparticles, Journal of Magnetism and Magnetic Materials 272–276 (2004) 1401–1403, https://doi.org/10.1016/j.jmmm.2003.12.139.
[96] R. Ianos, E.A. Moaca, A. Caprarua, R. Lazau, C. Pacurariu, Maghemite, gamma-Fe2O3, nanoparticles preparation via carbon-templated solution combustion synthesis, Ceramics International 44 (2018) 14090–14094, https://doi.org/10.1016/j.ceramint.2018.04.258.
[97] P.V. Medvedev, M.A. Soldatov, V.V. Shapovalov, A.A. Tereshchenko, I. E. Gorban', A.G. Fedorenko, A.V. Soldatov, Analysis of the local atomic structure of the MIL-88a metal–organic framework by computer simulation using XANES data, JETP Letters 108 (2018) 318–325, https://doi.org/10.1134/S0021364018170083.
[98] C. Piquer, M.A. Laguna-Marco, A.G. Roca, R. Boada, C. Guglieri, J. Chaboy, Fe K-edge X-ray absorption spectroscopy study of nanosized nominal magnetite, The Journal of Physical Chemistry C 118 (2014) 1332–1346, https://doi.org/10.1021/jp4104992.
[99] F. Menil, Systematic trends of the 57Fe Mössbauer isomer shifts in (FeOn) and (FeFn) polyhedra. Evidence of a new correlation between the isomer shift and the inductive effect of the competing bond T-X (→ Fe) (where X is O or F and T any element with a formal positive charge), Journal of Physics and Chemistry of Solids 46 (1985) 763–789, https://doi.org/10.1016/0022-3697(85)90001-0.
[100] F.J. Berry, D.J. Vaughan, Chemical Bonding and Spectroscopy in Mineral Chemistry, Chapman and Hall, 1985, p. 326.
[101] S. Bedanta, W. Kleemann, Supermagnetism, Journal of Physics D: Applied Physics 42 (2008), 013001, https://doi.org/10.1088/0022-3727/42/1/013001.
[102] Y.V. Knyazev, D.A. Balaev, V.L. Kirillov, O.A. Bayukov, O.N. Mart'yanov, Mossbauer spectroscopy study of the superparamagnetism of ultrasmall E-Fe2O3 nanoparticles, JETP LETTERS 108 (2018) 527–531, https://doi.org/10.1134/S0021364018200092.
[103] D.H. Jones, K.K.P. Srivastava, Many-state relaxation model for the Mössbauer spectra of superparamagnets, Physical Review B 34 (1986) 7542–7548, https://doi.org/10.1103/PhysRevB.34.7542.
[104] M. Tadic, D. Markovic, V. Spasojevic, V. Kusigerski, M. Remskar, J. Pirnat, Z. Jagličić, Synthesis and magnetic properties of concentrated α-Fe 2O 3 nanoparticles in a silica matrix, Journal of Alloys and Compounds - J ALLOYS COMPOUNDS 441 (2007) 291–296, https://doi.org/10.1016/j.jallcom.2006.09.099.
[105] A. Shavel, B. Rodríguez-González, M. Spasova, M. Farle, L.M. Liz-Marzán, Synthesis and characterization of iron/iron oxide core/shell nanocubes, Advanced Functional Materials 17 (2007) 3870–3876, https://doi.org/10.1002/adfm.200700494.
[106] K.L. Pisane, S. Singh, M.S. Seehra, Unusual enhancement of effective magnetic anisotropy with decreasing particle size in maghemite nanoparticles, Applied Physics Letters 110 (2017), 222409, https://doi.org/10.1063/1.4984903.
[107] K. Enpuku, A.L. Elrefai, T. Yoshida, T. Kahmann, J. Zhong, T. Viereck, F. Ludwig, Estimation of the effective magnetic anisotropy constant of multi-core based magnetic nanoparticles from the temperature dependence of the coercive field, Journal of Applied Physics 127 (2020), 133903, https://doi.org/10.1063/1.5144713.
[108] D.A. Balaev, A.A. Krasikov, A.A. Dubrovskiy, S.I. Popkov, S.V. Stolyar, O. A. Bayukov, R.S. Iskhakov, V.P. Ladygina, R.N. Yaroslavtsev, Magnetic properties of heat treated bacterial ferrihydrite nanoparticles, Journal of Magnetism and Magnetic Materials 410 (2016) 171–180, https://doi.org/10.1016/j.jmmm.2016.02.059.
[109] N.J.O. Silva, V.S. Amaral, L.D. Carlos, B. Rodríguez-González, L.M. Liz-Marzán, T. S. Berquó, S.K. Banerjee, V. de Zea Bermudez, A. Millán, F. Palacio, Evidence of random magnetic anisotropy in ferrihydrite nanoparticles based on analysis of statistical distributions, Physical Review B 77 (2008), 134426, https://doi.org/10.1103/PhysRevB.77.134426.
[110] S. Mondal, M.E. De Anda Reyes, U. Pal, Plasmon induced enhanced photocatalytic activity of gold loaded hydroxyapatite nanoparticles for methylene blue degradation under visible light, RSC Advances 7 (2017) 8633–8645, https://doi.org/10.1039/C6RA28640B.
[111] T. Zhang, T. Oyama, A. Aoshima, H. Hidaka, J. Zhao, N. Serpone, Photooxidative N-demethylation of methylene blue in aqueous TiO2 dispersions under UV irradiation, Journal of Photochemistry and Photobiology A: Chemistry 140 (2001) 163–172, https://doi.org/10.1016/S1010-6030(01)00398-7.
[112] H.J.H. Fenton, LXXIII.—oxidation of tartaric acid in presence of iron, Journal of the Chemical Society, Transactions 65 (1894) 899–910, https://doi.org/10.1039/CT8946500899.
[113] R. Ameta, K. Chohadia, A.A. Jain, P.B. Punjabi, Chapter 3 - fenton and photo-fenton processes, in: S.C. Ameta, R. Ameta (Eds.), Advanced Oxidation Processes for Waste Water Treatment, Academic Press, 2018, pp. 49–87.
[114] S.M. Kim, A. Vogelpohl, Degradation of organic pollutants by the photo-fenton-process, Chem. Eng. Technol. 21 (1998) 187–191. 10.1002/(SICI)1521-4125(199802)21:2<187::AID-CEAT187>3.0.CO;2-H.